Supplementary Information

SUPPLEMENTARY METHODS

Mean-Field Model Equations of Cortical Electrodynamics The mean excitatory and inhibitory potentials V_e and V_i of each simulated neural population in the mean-field model, positioned at a location $\overrightarrow{r} = (x, y)$, are described by:

$$
\begin{aligned}
\tau_b \frac{\delta V_b(\overrightarrow{r}, t)}{\delta t} =& V_b^{\text{rest}} + \Delta V_b^{\text{rest}} - V_b(\overrightarrow{r}, t) \\
&+ [\rho_e \psi_{eb}(\overrightarrow{r}, t) \Phi_{eb}(\overrightarrow{r}, t) + \rho_i \psi_{ib}(\overrightarrow{r}, t) \Phi_{ib}(\overrightarrow{r}, t)] \\
&+ D_{bb}^2 V_b(\overrightarrow{r}, t)
\end{aligned}
\tag{1}
$$

where presynaptic to postsynaptic directionality is indicated by the right arrow, the subscript e indicates a presynaptic excitatory neural population, the subscript i indicates a presynaptic inhibitory neural population, and the subscript b indicates either a postsynaptic excitatory or postsynaptic inhibitory neural population. The bracketed term in Eq. 1 represents voltage inputs via chemical synapses, and the final term in Eq. 1 represents voltage inputs from diffusive gap junction coupling. ^{2} is the 2D Laplacian operator. D_{bb} represents the strength of diffusive gap junction coupling between adjacent neurons, such that D_{ee} is gap junction coupling between excitatory populations and D_{ii} is gap junction coupling between inhibitory populations. Because there is far more abundant gap-junction coupling between inhibitory interneurons than excitatory neurons [1], D_{ee} is set to $D_{ii}/100$. D_{ii} is one of the key biological parameters we vary. For a given excitatory or inhibitory neural population, V_b^{rest} is the mean resting potential, τ_b is the soma time constant, and ρ_b is the strength of chemical synapse coupling, which is scaled by the following reversal-potential function ψ_{ab}:

$$
\psi_{ab}(\overrightarrow{r}, t) = \frac{V_a^{\text{rev}} - V_b(\overrightarrow{r}, t)}{V_a^{\text{rev}} - V_b^{\text{rest}}}
\tag{2}
$$

which equals one when a neuron is at its resting potential and equals 0 when the membrane potential equals the reversal potential. For excitatory AMPA receptors, $V_e^{\text{rev}} = 0$ mV, and for inhibitory GABA receptors, $V_i^{\text{rev}} = -70$ mV. The Φ_{ab} functions in Eq. 1 describe postsynaptic spike-rate fluxes:

$$\left(\frac{\delta}{\delta t} + \gamma_e\right)^2 \Phi_{eb}(\overrightarrow{r}, t) = \gamma_e^2 [N_{eb}^{\alpha} \phi_{eb}^{\alpha}(\overrightarrow{r}, t) + N_{eb}^{\beta} Q_e(\overrightarrow{r}, t)$$
$$+ \phi_{eb}^{\text{sc}}(\overrightarrow{r}, t) + \phi_{eb}^{\alpha,\text{het}}(\overrightarrow{r}, t)], \tag{3}$$

$$\left(\frac{\delta}{\delta t} + \gamma_i\right)^2 \Phi_{ib}(\overrightarrow{r}, t) = \gamma_i^2 N_{ib}^{\beta} Q_i(\overrightarrow{r}, t) \tag{4}$$

where the α superscript corresponds to inputs from long-range myelinated axons: N_{eb}^{α} is the number of axonal inputs to a population and ϕ_{eb}^{α} is long-range spike-rate flux. The β superscript corresponds to inputs from short-range chemical synapses, such that N_{eb}^{β} is the number of local chemical synapses in a neural population. $Q_{e,i}$ is the local spike-rate flux, and $\phi_{eb}^{\alpha,\text{het}}$ is a heterogeneous flux input. ϕ_{eb}^{sc} is white noise, taken to represent random inputs to the cortex from subcortical sources (e.g. sensory inputs); note that the inclusion of a noise term means that the above equations are stochastic differential equations, and that analyses of the ground-truth chaoticity of the model (i.e. its largest Lyapunov exponent) are performed exclusively using the non-stochastic components of the model equations; estimates of chaoticity using the 0-1 test (see below) are performed with the model's noise input turned on, so as to better assess the viability of detecting changing levels of chaoticity in real cortical recordings. γ_i is the inhibitory rate constant and γ_e is the excitatory rate constant, which we vary so as to the study the effect of excitation and inhibition on chaos in the model. See Steyn-Ross, Steyn-Ross, and Sleigh [2] for more details on the model equations. Other than the inhibitory gap-junction coupling strength D_{ii}, the excitatory rate constant γ_e, and the inhibitory rate constant γ_i (all of which we vary in our parameter sweep), all parameters in our

simulations are unchanged from the original model, and are taken from the empirical literature [2]. D_{ii} was varied from 0.1 to 0.7 in steps of 0.2, and both γ_e and γ_i were varied from 0.945 to 1.05 in steps of 0.005. Of the 1,936 resulting simulations, 1,160 yielded flat, non-oscillatory activity, likely reflecting stable fixed points of the model; these fixed point solutions were excluded from all analyses, because these non-oscillatory solutions would likely yield high estimates of Lempel-Ziv complexity simply due to the information-richness of the noise perturbations rather than of the underlying system dynamics. This left 776 unique model simulations of oscillatory behavior. Based on prior work [2], the waking conscious simulation corresponded to $\gamma_e = 1$, $\gamma_i = 1$, and $D_{ii} = 0.7$. The anesthesia simulation corresponded to $\gamma_e = 1$, $\gamma_i = 1.015$, and $D_{ii} = 0.5$, and the seizure simulation corresponded to $\gamma_e = 1$, $\gamma_i = 1$, and $D_{ii} = 0.1$. The nearest-to-criticality and maximally information-rich state of the model (see SI Appendix, Figs. S2, S4) corresponded to $\gamma_e = 1.04$, $\gamma_i = 1$, and $D_{ii} = 0.5$. The model equations were integrated using a forward time center spaced first-order Euler method, with an integration step of 0.2 ms. Simulated electrodynamics were then downsampled to a sampling frequency of 500 Hz, and the final 10 seconds (i.e. 5,000 time-points) were extracted from the downsampled data, so as to perfectly match the length and sampling frequency of the ECoG and MEG datasets analyzed in this paper.

Calculating Largest Lyapunov Exponents in the Mean-Field Model The ground-truth chaoticity of a system is determined by its largest Lyapunov exponent, which is the rate of divergence between initially similar trajectories in a system's phase space. A positive largest Lyapunov exponent means that a system is chaotic, because it indicates exponential divergence of initially similar system states. A negative largest Lyapunov exponent indicates periodicity, because it indicates exponentially fast convergence of initially similar states. A largest Lyapunov exponent near 0 corresponds to edge-of-chaos criticality, and near-0 exponents indicate that a system is near the edge-of-chaos critical point. The larger the largest Lyapunov exponent, the more strongly chaotic the system is. Following Steyn-Ross, Steyn-Ross, and Sleigh [2], we estimate the largest Lyapunov exponent of the mean-field model by simulating two runs of its deterministic component (i.e., with

its noise inputs turned off), with slightly different initial conditions. The divergence between the excitatory firing rate of run 1 $Q_e^{(1)}$ and run 2 $Q_e^{(2)}$ is estimated as their summed squared-difference $\epsilon(t)$ down the midline of the simulated cortical grid:

$$\epsilon(t) = \sum_{i=1}^{N_x} (Q_e^{(1)}(x_i, t) - Q_e^{(2)}(x_i, t))^2 / \epsilon^{\mathrm{max}} \tag{5}$$

where ϵ^{max} is a normalization parameter, which equals the maximum possible difference between the two runs:

$$\epsilon^{\mathrm{max}} = N_x \left(\max(Q_e^{(1)}) - \min(Q_e^{(2)}) \right)^2 \tag{6}$$

where N_x=120, i.e. the number of simulated neural populations in the cortical sheet. The rate of divergence between the two runs $\epsilon(t)$ is directly related to the largest Lyapunov exponent Λ of the system:

$$\epsilon(t) = \epsilon(0)\exp(\Lambda t) \tag{7}$$

where $\epsilon(0)$ is the distance between the two runs at $t = 0$. The largest Lyapunov exponent can therefore be estimated by measuring the slope of $\ln\epsilon(t)$-versus-t. A positive slope indicates a positive largest Lyapunov exponent (and therefore chaotic dynamics), a negative slope indicates periodicity, and a flat slope indicates edge-of-chaos criticality.

Modified 0-1 chaos test The modified 0-1 test takes a univariate time-series $\boldsymbol{\phi}$, and uses that time-series to drive the following two-dimensional system:

$$p(n+1) = p(n) + \phi(n)\cos cn$$
$$q(n+1) = q(n) + \phi(n)\sin cn \tag{8}$$

where c is a uniformly distributed random variable bounded between 0 and 2π. For a given c, the solution to Eq. 1 yields:

$$p_c(n) = \sum_{j=1}^{n} \phi(j)\cos jc$$
$$q_c(n) = \sum_{j=1}^{n} \phi(j)\sin jc \tag{9}$$

If the time-series $\boldsymbol{\phi}$ is periodic, the motion of $\mathbf{p}$ and $\mathbf{q}$ is bounded, while if the time-series $\boldsymbol{\phi}$ is chaotic, $\mathbf{p}$ and $\mathbf{q}$ display asymptotic Brownian motion. The time-averaged mean square displacement of $\mathbf{p}$ and $\mathbf{q}$ is

$$M_c(n) = \frac{1}{N} \sum_{j=1}^{N} ([p_c(j+n) - p_c(j)]^2 + [q_c(j+n) - q_c(j)]^2) + \sigma\eta_n. \tag{10}$$

where η_n is a uniformly distributed random variable between $[-\frac{1}{2}, \frac{1}{2}]$ and σ controls the amplitude of the added random variable η_n. We set σ to 0.5 and normalized the standard deviation of all signals to 0.5, based on our previously published analyses [3] of the effect of different parameter values for 0-1 test performance across diverse datasets. To compute the degree of chaos using a single statistic K, the 0-1 test calculates the growth rate of the mean squared displacement of the two-dimensional system in Eq. 5 using a correlation coefficient:

$$K_c = \text{corr}(n, M_c(n)) \tag{11}$$

K is computed for 100 different values of c, uniformly randomly sampled between 0 and 2π, and the output of the test is the median K across different values of c. For both our real and simulated cortical activity, we calculated K for every channel in a trial, and estimated that trial's level of chaoticity as the median K-statistic across all channels in that trial.

Epilepsy data Surface ECoG data from nine epilepsy patients were downloaded from the European Epilepsy Database [4]. Of these, only two subjects experienced fully generalized seizures (in both cases, seizures were focal with secondary generalizations). Subject 1 was a 42 year old male with epilepsy caused by right cortical dysplasia, and who was receiving the anticonvulsant medication lamotrigine. The subject had six intracranial electrode strips (26 electrodes in total) placed over right lateral temporal cortex to monitor seizure focus. Subject 2 was a 14 year old female with cryptogenic epilepsy (i.e. unknown cause) who was receiving the anticonvulsant medications valproate and topiramate; the subject had one grid and six electrode strips (96 electrodes total) placed over left temporal and lateral left temporal cortex to monitor seizure focus. Signals from both subjects were recorded at a sampling rate of 1024 Hz. Data were demeaned, detrended, and band-stop filtered at 50 Hz and harmonics (the line noise frequency in Europe). Data were resampled to 500 Hz, divided into 10-second trials, and re-referenced to the common average. For the seizure state, we only included trials for which seizures were fully generalized across all channels for the entire trial duration. The data were then visually inspected for artifacts. Data from electrodes with consistent motion or drift artifacts were removed, and 10-second trials with large motion artifacts spanning multiple electrodes were removed.

Additionally, a magnetoencephalograpy (MEG) recording of one patient's generalized absence seizure, previously published by Dominguez and colleagues [5], was re-analyzed. Data were provided by D.M.M. Note that MEG datasets were recorded for two other epilepsy patients by Dominguez and colleagues, but that these were for tonic seizures; the muscle convulsions during these tonic episodes produced large motion artifacts in the MEG data, which rendered analysis of

low-frequency periodicity impossible. These datasets were therefore not analyzed. The patient whose data were re-analyzed in the present paper (Seizure Subject 3 in SI Appendix, Figs. S2-4) was an 18 year-old female who was receiving a low dose of valproate, and with no reported structural abnormalities or prior brain surgery. Data from this patient were recorded at 625 Hz using a CTF Omega 151 channel whole-head system (CTF Systems, Port Coquitlam, British Columbia, Canada). Data were split into 10-second trials, demeaned, detrended, and bandstop filtered at 60 Hz and harmonics (the line noise frequency in Canada, where data were collected). Data were then visually inspected. Consistently motion or drift artifact-affected channels were removed, and trials with large motion artifacts across channels were removed. Data were then downsampled to 500 Hz. We then ran an independent components analysis on the data, and removed components that corresponded to ocular or cardiac artifacts. See SI Appendix, Fig. S15 for 10-second time-traces of these subjects' cortical electrodynamics during generalized seizures.

Human Anesthesia Data Electrode placement for our human anesthesia subjects was determined only by clinical criteria (Ad-Tech, SEEG: 5 mm inter-electrode spacing; Integra, Grids: 1 cm, 5 or 4 mm spacing). ECoG data were recorded using a Nihon Kohden recording system (256 channel amplifier, model JE120A), analogue-filtered above 0.01 Hz and digitally sampled at 5 kHz.

Patient 1 (Human Anesthesia Subject 1 in SI Appendix, Figs. S2-4) was a right-handed 25 year-old female with a diffuse lesion in the right supplementary motor area. The patient had one 8x8 grid placed over the right frontal lobe, and two 2x5 anterior interhemisphere bilateral grids and two 2x8 posterior interhemisphere bilateral grids, for a total of 116 cortical contacts. See SI Appendix, Fig. S16 for MRI scans with Patient 1's cortical grids. The patient received 100 mg of propofol and 100 mcg of fentanyl prior to surgical resection of their epileptic focus. Their "waking conscious" data consisted of the twenty minutes prior to anesthetic induction, and their "anesthesia" data consisted of the twenty minutes following the loss of responsiveness to verbal commands.

Patient 2 (Human Anesthesia Subject 2 in SI Appendix, Figs. S2-4) was a 46 year-old, right-handed female with a lesion in the left supplemantary motor area. The patient had one 8x8 grid placed over the left frontal lobe, one 2x8 strip placed over left medial cortex, and one 2x8 strip placed over right medial cortex, for a total of 96 contacts. See SI Appendix, Fig. S16 for MRI scans with Patient 2's cortical grids. The patient received 140 mg of propofol and 50 mcg of fentanyl prior to surgery; at loss of consciousness, the patient received 50 mg of the muscle relaxant rocuronium; four minutes after loss of consciousness, the patient began receiving sevoflurane (another GABAergic anesthetic) for maintenance of anesthesia; note that the predictions of the mean-field model regarding the anesthesia state still hold for a combination of propofol and sevoflurane, as the model predictions should pertain to any GABAergic anesthetic. The patient's "waking conscious" data consisted of the 19 minutes prior to anesthetic induction, and their "anesthesia" data consisted of the 16.8 minutes following the loss of responsiveness to verbal commands.

Patient 3 (Human Anesthesia Subject 3 in SI Appendix, Figs. S2-4) was a 20 year-old right-handed female who had previously received a left temporal lobectomy. The patient had one 4x8 grid placed over left frontal cortex, another 4x4 grid over left frontal cortex, a 2x6 grid over the temporal lobe, and one 8x8 grid with contacts over parts of parietal, temporal, and occipital cortices, for a total of 124 surface electrodes. See SI Appendix, Fig. S16 for MRI scans with Patient 3's ECoG grids. The patient received 150 mg of propofol and 100 mcg of fentanyl prior to surgical resection of their epileptic focus. Their "waking conscious" data consisted of the eight minutes prior to anesthetic induction, and their "anesthesia" data consisted of the 10.17 minutes following the loss of responsiveness to verbal commands.

Signals for all three patients were recorded at a sampling rate of 1,000 Hz. Epileptic activity was assessed by an experienced neurologist (R.T.K) and removed. Data were split into 10-second trials, demeaned, band-stop filtered at 60 Hz and harmonics (the line noise frequency in the United States, where data were collected), detrended, downsampled to 500 Hz, and re-referenced to the

common average. Data were then visually inspected for artifacts. Data from electrodes with consistent drift or motion artifacts were removed, and 10-second trials with large motion artifacts spanning multiple electrodes were removed.

Macaque Anesthesia Data Open-source ECoG recordings spanning the left cortices (including occipital, parietal, temporal, and frontal lobes) of two male macaques were downloaded from Neurotycho.org [6]. See SI Appendix, Fig. S16 for an MRI scan showing the electrode placement of Macaques 1 and 2. Data were collected during awake/resting and propofol anesthesia states. The macaques were seated with head and arm movement restricted. Macaque 1 (Macaque Anesthesia Subject 1 in SI Appendix, Figs. S2-4) was intravenously administered 5.2 mg/kg of propofol, and Macaque 2 (Macaque Anesthesia Subject 2 in SI Appendix, Figs. S2-4) was intravenously administered 5 mg/kg of propofol. Loss of consciousness was determined by the emergence of low-frequency oscillations and the cessation of responses to physical stimuli. All data for the propofol condition are from the macaques' unconscious state, and all data from the awake condition are from the macaques' eyes-open state (i.e., data for which the eyes were covered were excluded). Signals were recorded at a sampling rate of 1,000 Hz. Data were split into 10-second trials, demeaned, band-stop filtered at 50 Hz and harmonics (the line noise frequency in Japan, where data were collected), detrended, downsampled to 500 Hz, and re-referenced to the common average. Data were then visually inspected for motion artifacts. Data from electrodes with consistent artifacts were removed, and 10-second trials with artifacts spanning multiple electrodes were removed.

Human Lysergic Acid Diethylamide Data Previously published [7] MEG recordings of nineteen humans following intravenous administration of either 75 μg of lysergic acid diethylamide (LSD) or a saline placebo were re-analyzed. These data were provided by S.M. and R.C. Data from three subjects were excluded because of persistent motion or drift artifacts in their MEG signal across most trials. Of the sixteen remaining subjects, three were females, and the average age was 32.06 (with a standard deviation of 7.71 years). Due to the slow pharmacodynamics of LSD, MEG data

were recorded four hours after drug administration. Subjects lay in a supine position during data acquisition. MEG signals were recorded using a CTF 275-channel radial gradiometer system with a sampling frequency of 1200 Hz. After the MEG recordings were collected, visual analogue scale ratings of the intensity of the LSD experience (on a scale from 0 to 20 in increments of 1) were presented to subjects on a projection screen visible from inside the scanner, which the subjects completed via button press (see Carhart-Harrris et al [7] for more details). MEG data were split into 10-second trials, demeaned, detrended, and bandstop filtered at 50 Hz and harmonics (the line noise frequency in the United Kingdom, where data were collected). Data were then visually inspected. Consistently motion or drift artifact-affected channels were removed, and trials with large motion artifacts across channels were removed. Data were then downsampled to 500 Hz. We then ran an independent components analysis on the data, and removed components that corresponded to ocular or cardiac artifacts.

Clinical DOC data Data were collected from four traumatic brain injury (TBI) patients admitted at the UCLA Ronald Reagan University Medical Center intensive care unit (ICU). Several criteria were applied for participation in the study in order to limit the investigation to those patients recovering from unconsciousness. Inclusion criteria: Glasgow Coma Scale (GCS) score ≤ 8 or an admission GCS score of 9-14 with computed tomography (CT) evidence of intracranial bleeding. Exclusion criteria: GCS > 14 with non-significant head CT, history of neurological disease or TBI, and brain death. The UCLA institutional review board approved the study. Informed consent was obtained according to local regulations. To manage symptoms and/or reduce cerebral metabolism, medications were administered to patients as needed, noted on a daily basis and sorted into appropriate categories: propofol, barbiturates, benzodiazepines, opioids, and dissociative anesthetics. Behavioral assessments were performed several times daily in the ICU and used the GCS to assess patients' conscious state. EEG data were recorded continuously (Cz reference) at a sampling rate of 250 Hz for several days or longer while patients were in the ICU. After data acquisition with Persyst software (Persyst Development Corporation, Solana Beach, CA, USA), data were exported

in EDF format to MATLAB (The MathWorks, Inc., Natick, MA, USA) for analysis.

To analyze patients during periods of both high responsiveness (conscious) and minimal responsiveness (unconscious), we extracted 60 minutes of EEG from 13 channels common to all patients (Fp1, Fp2, F7, F8, T3, C3, Cz, C4, T4, T5, O1, O2, T6) at timepoints corresponding to consciousness, defined as GCS motor score ≥ 5 or GCS verbal score ≥ 4 [8,9], and unconsciousness. EEG sections were spaced a minimum of 12 hours apart according to the following procedure, applied separately for conscious and unconscious data: 1) sorting each patient's GCS scores from or high to low (conscious) or low to high (unconscious), 2) appending the highest (conscious) or lowest (unconscious) score to a second list, and 3) crawling down the first list of GCS scores and adding each timepoint that was at least 12 hours from any timepoint on the second list to the second list. 60-minute EEG sections were then extracted from the second list's timepoints in order to sample the desired periods of consciousness and unconsciousness. Data were split into 10-second trials, demeaned, detrended, and re-referenced to the common average. Data were then visually inspected for artifacts. Data from electrodes with consistent drift or motion artifacts were removed, and 10-second trials with large motion artifacts spanning multiple electrodes were removed. We then ran an independent components analysis on the data to remove ocular or cardiac artifacts.
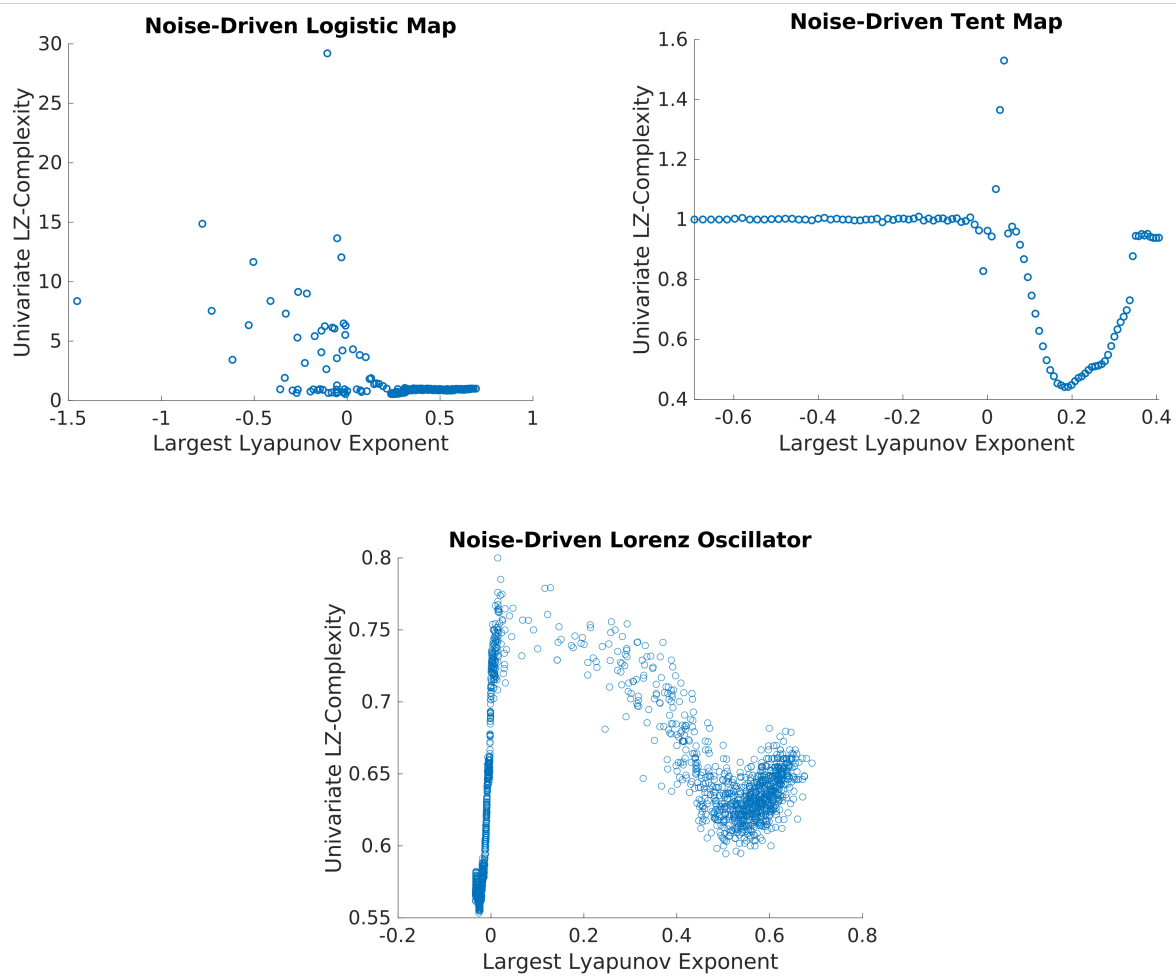
SUPPLEMENTARY FIGURES

Fig. S1: (Caption on the following page.)

Fig. S1: To our knowledge, the relationship between Lempel-Ziv complexity and edge-of-chaos criticality (i.e., a largest Lyapunov exponent of zero) has not previously been studied in any dynamical system. Most prior information-theoretic analyses of dynamics at this critical point have utilized Shannon entropy, mutual information, or transfer entropy; we instead chose to use Lempel-Ziv complexity because of its well-validated ability to track conscious level in multiple species (see Introduction). Therefore, in order to ensure that the simulated behavior we plotted in Fig. 2 is generalizable to other systems, we studied the behavior of Lempel-Ziv complexity in three other noise-driven dynamical systems for which (deterministic) largest Lyapunov exponents can be estimated with far greater accuracy than is possible in the high-dimensional mean-field model of cortical electrodynamics analyzed here. The first system we studied is the noise-driven logistic map (top left), whose behavior is governed by the equation $x_{i+1} = 1 - rx_i(1 - x_i)^2 + \mu\epsilon$, where r is a parameter, ϵ_n is white noise with mean 0 and standard deviation 1, and μ is a parameter which controls the amplitude of the noise. The largest Lyapunov exponent of the logistic map equals $\lim_{n\to\infty} \frac{1}{n} \sum_{i=1}^{n-1} |2ax_i|$, and can be precisely estimated using the iterative method. We varied the parameter r from 1.5 to 2 in steps of 0.001 in order to produce dynamics on both sides of the edge-of-chaos critical point. The second system we studied is the noise-driven tent map (top right), which is a discrete-time system governed by the following equation:

$$x_{n+1} = \begin{cases} rx_n + \mu\epsilon & x_n < \frac{1}{2} \\ r(1 - x_n) + \mu\epsilon & x_n \geq \frac{1}{2} \end{cases} \tag{13}$$

where r is a parameter, ϵ_n is white noise with mean 0 and standard deviation 1, and μ is a parameter which controls the amplitude of the noise. The deterministic largest Lyapunov exponent of the tent map is precisely $ln(r)$, and can thus be calculated with perfect accuracy. We varied r from 0.5 to 1.5 in steps of 0.01 to produce dynamics in both the periodic and chaotic phases. The third system we studied is the noise-driven Lorenz system, which is a continuous-time three-dimensional system governed by the following equations: $\frac{dx}{dt} = \sigma(y - x) + \mu\epsilon$, $\frac{dy}{dt} = x(\rho - z) - y$, and $\frac{dz}{dt} = xy - \beta z$, where σ, ρ, and β are parameters, and where ϵ_n is again white noise with mean 0 and standard deviation 1 and μ is a parameter which controls the amplitude of the noise. These equations were integrated using the Fourth Order Runge-Kutta method with an integration step of 0.01. We set $\sigma = 10$, $\beta = \frac{8}{3}$, and varied ρ from 23 to 25 in steps of 0.001. As was the case for both the logistic and tent maps, we chose this parameter range because it produces dynamics on both sides of the edge-of-chaos critical point. To get a single time-series from the model, we took a linear combination of all three variables. Ground-truth Lyapunov exponents of the Lorenz oscillator were estimated using Ramasubramanian's algorithm[10]. For all three systems, we set the noise amplitude μ to 0.001. We found that univariate Lempel-Ziv complexity clearly peaked near the edge-of-chaos critical point (largest Lyapunov exponent of zero) in all three systems, consistent with what we observed in the mean-field model of low-frequency cortical electrodynamics (Fig. 2).
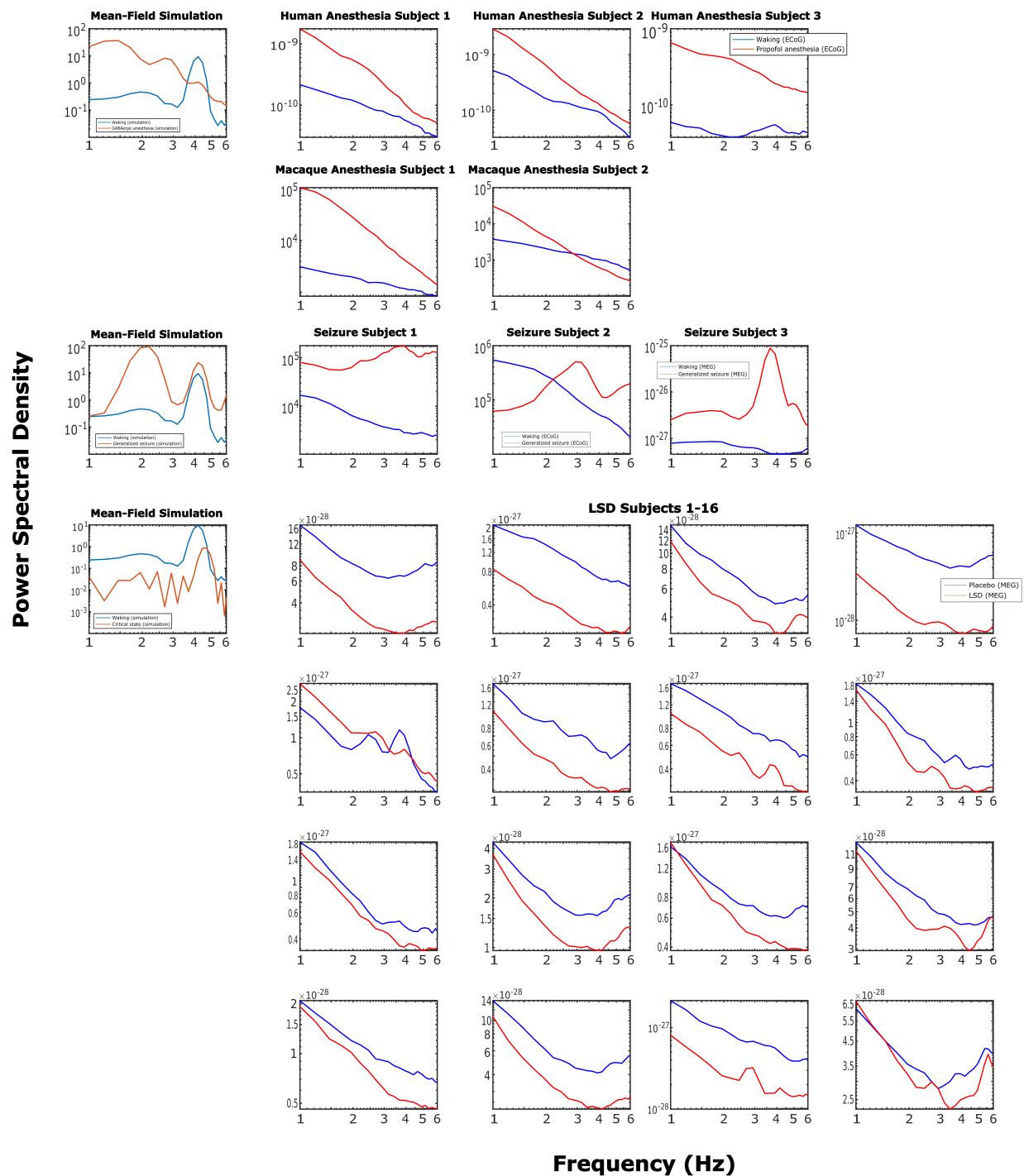
Fig. S2: (Caption on the following page.)

Fig. S2: We here plot the low-frequency power spectra of our real and simulated cortical electrody-namics in different states. For simulated data, we plot the median power spectrum across simulated cortical populations, and for empirical data, we plot the cross-channel median of each channel's cross-trial median power spectrum. Note that we here focus on 1-6 Hz, because the mean-field model only simulates oscillations intrinsic to the cortex in this range (without, for example, incor-porating thalamic inputs, which are thought to underlie oscillations in the 8-12 Hz range). This was also the range over which we used the FOOOF algorithm to search for the frequencies of slow oscillations in our data. Note that the use of different datasets and imaging modalities led to wide variation in spectral power (for e.g., note that the spectral power of the MEG datasets was far lower than the spectral power of the ECoG datasets). In both the mean-field model and ECoG data, we see an increase in power and a steepening of spectral slope in the anesthesia state. Note that the model appears to have a peak at 4 Hz in the waking state that is absent in the real data, but that this apparent absence in real data is likely an artifact induced by averaging over channels whose slow oscillations extend over a range of frequencies (Figs. S3-S4). For the generalized seizure state, we see clear peaks between 3-4 Hz for both the model and real data. Though the model spectrum also includes a peak at 2 Hz that is apparently absent in the empirical data, note that this absence may again be an artifact of averaging over diverse channels (Figs. S3-S4). Finally, we compared power spectra in the LSD state to the power spectrum of the most information-rich and nearest-to-criticality state of the model (i.e., the only model parameter configuration that produced dynamics with a normalized Lempel-Ziv complexity greater than 0.99 for all three variants of Lempel-Ziv complexity as well as an absolute largest Lyapunov exponent less than 0.1). Like the LSD state, this parameter configuration - which corresponded to an increase in cortical excitability coupled with a slight decrease in the strength of gap junction coupling between inhibitory interneurons - resulted in reduced low-frequency power relative to the waking state. The similarities between the critical, maximally information-rich state of the model and the LSD state suggest possible follow-up work regarding potential molecular mechanisms of psychedelics - see Supplementary Note 2.
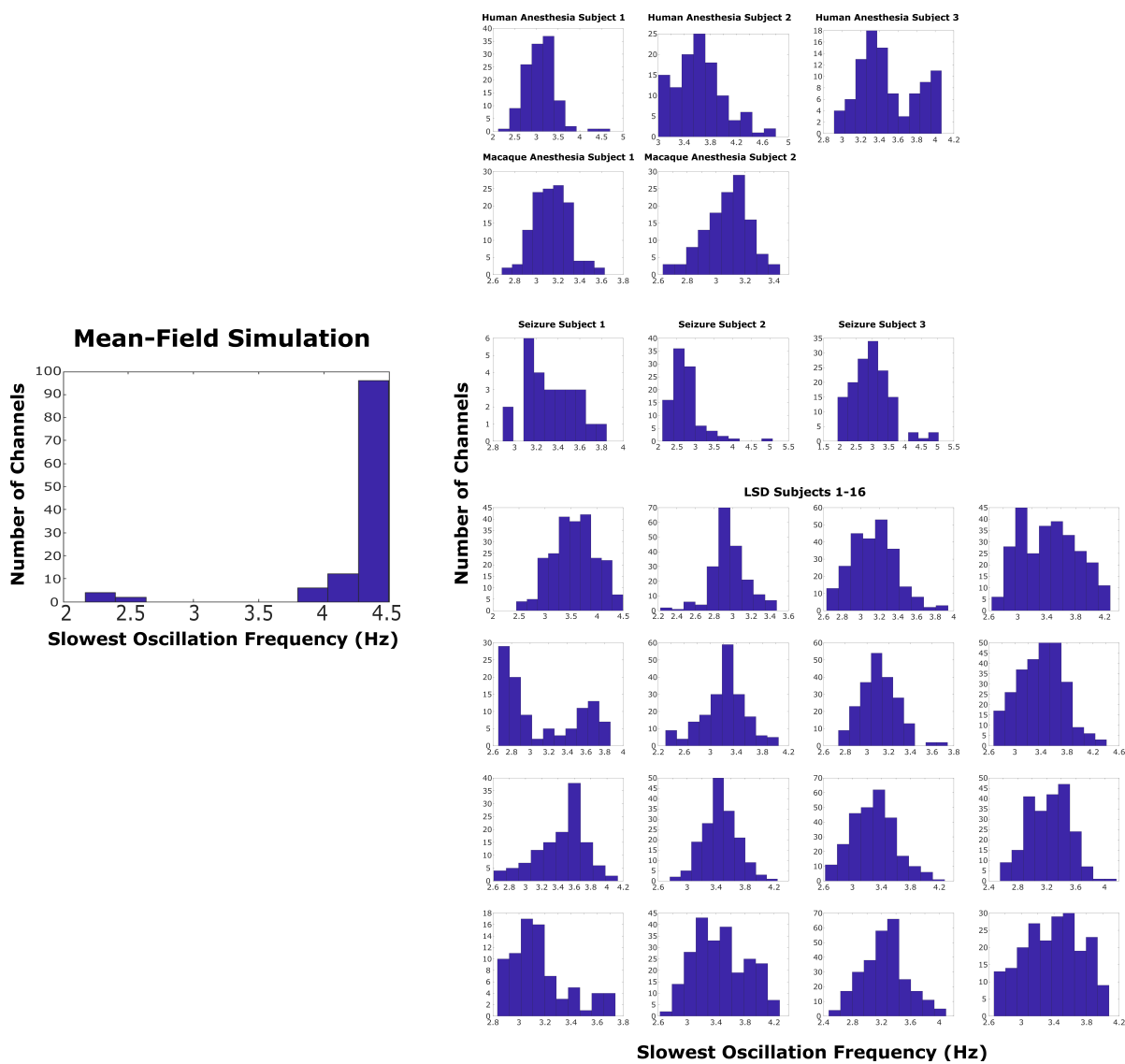
Human Anesthesia Subject 1   Human Anesthesia Subject 2   Human Anesthesia Subject 3

Macaque Anesthesia Subject 1   Macaque Anesthesia Subject 2

Mean-Field Simulation

Number of Channels

Slowest Oscillation Frequency (Hz)

Seizure Subject 1   Seizure Subject 2   Seizure Subject 3

LSD Subjects 1-16

Number of Channels

Slowest Oscillation Frequency (Hz)

Fig. S3: (Caption on the following page.)

Fig. S3: The mean-field model used in this paper simulates the electrodynamics of a homogeneous patch of cortex, and as such produces electrodynamic oscillations with similar frequencies. Reflecting this, the FOOOF algorithm (as described in our Materials and Methods) identifies a relatively narrow range of slowest oscillation frequencies in the waking state of the model between 1-6 Hz (left). Our empirical recordings of cortical electrodynamics, however, were collected across heterogenous parts of cortex, and it is known that different parts of cortex produce electrodynamic oscillations at varying frequencies, which is one of the motivations behind the development of the FOOOF algorithm[11]. Thus, as expected, the FOOOF algorithm identified a broader range of slowest oscillation frequencies during normal waking states across the cortex of each one of our subjects (right). Therefore, in Fig. S4, we repeated the cross-state comparisons of power spectra as reported in Fig. S2, but looking exclusively at channels whose slowest oscillation frequencies during normal waking states were close to those of the waking state of the mean-field model.
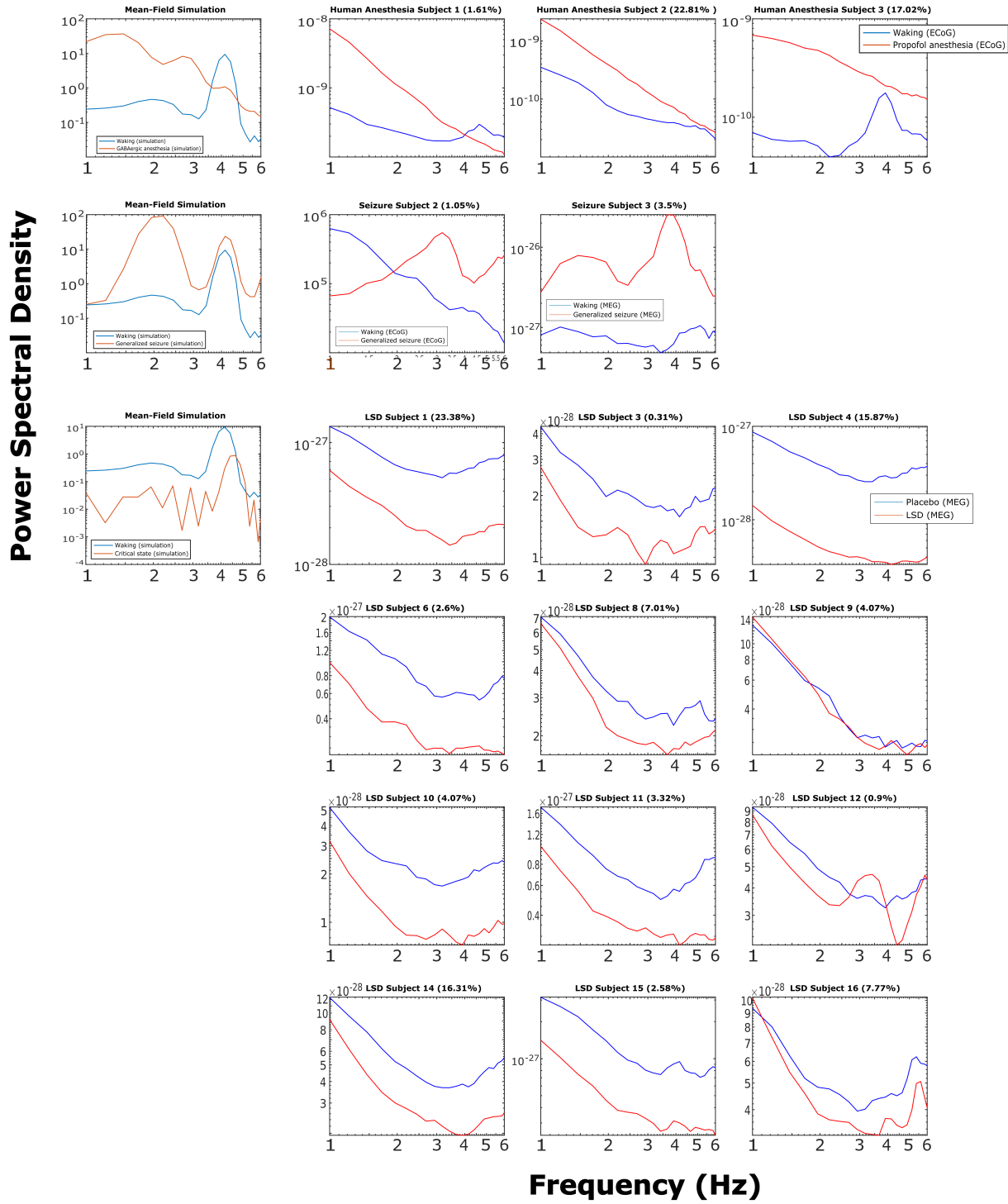
Fig. S4: (Caption on the following page.)

Fig. S4: To compare the power spectra of channels whose oscillatory behavior during normal waking states more closely matched that of the waking state of the mean-field model, we identified channels whose cross-trial median slowest oscillation frequencies during wake states (Fig. S3, right) were within $\pm 10\%$ of the median of the slowest oscillation frequencies of the waking state of the model (Fig. S2, left), which was 4.3 Hz. In other words, we only looked at channels whose slowest oscillation fell between 3.87 and 4.73 Hz. Note that several subjects had no channels whose slowest identified oscillation frequencies were within this range, and so are not plotted here. For each subject whose results are plotted here, we additionally indicate the percentage of their cortical channels that fell within this frequency range during normal waking states. Looking at just these channels, we found a 3-4 Hz rise above the background power spectrum during waking states for most subjects, which better matches the mean-field model, and also observed spectral changes during altered states (i.e., anesthesia, generalized seizures, and LSD) that likewise matched both the model and what we observed for the median across all channels (Fig. S2). We also found that the power spectrum of Seizure Subject 3's generalized seizure more closely matched the power spectrum of the simulated seizure. Note that in all other analyses in this paper, we included all channels for which any oscillation was identified in the 1-6 Hz range when estimating low-frequency chaoticity, rather than the far narrower range of 3.87-4.73 Hz analyzed in this figure; this analysis is only meant to illustrate that some of the minor apparent mismatches between empirical neural power spectra and the model's power spectra in Fig. S2 are due to averaging across patches of cortex with heterogeneous electrodynamic oscillation frequencies (as in Fig S2).
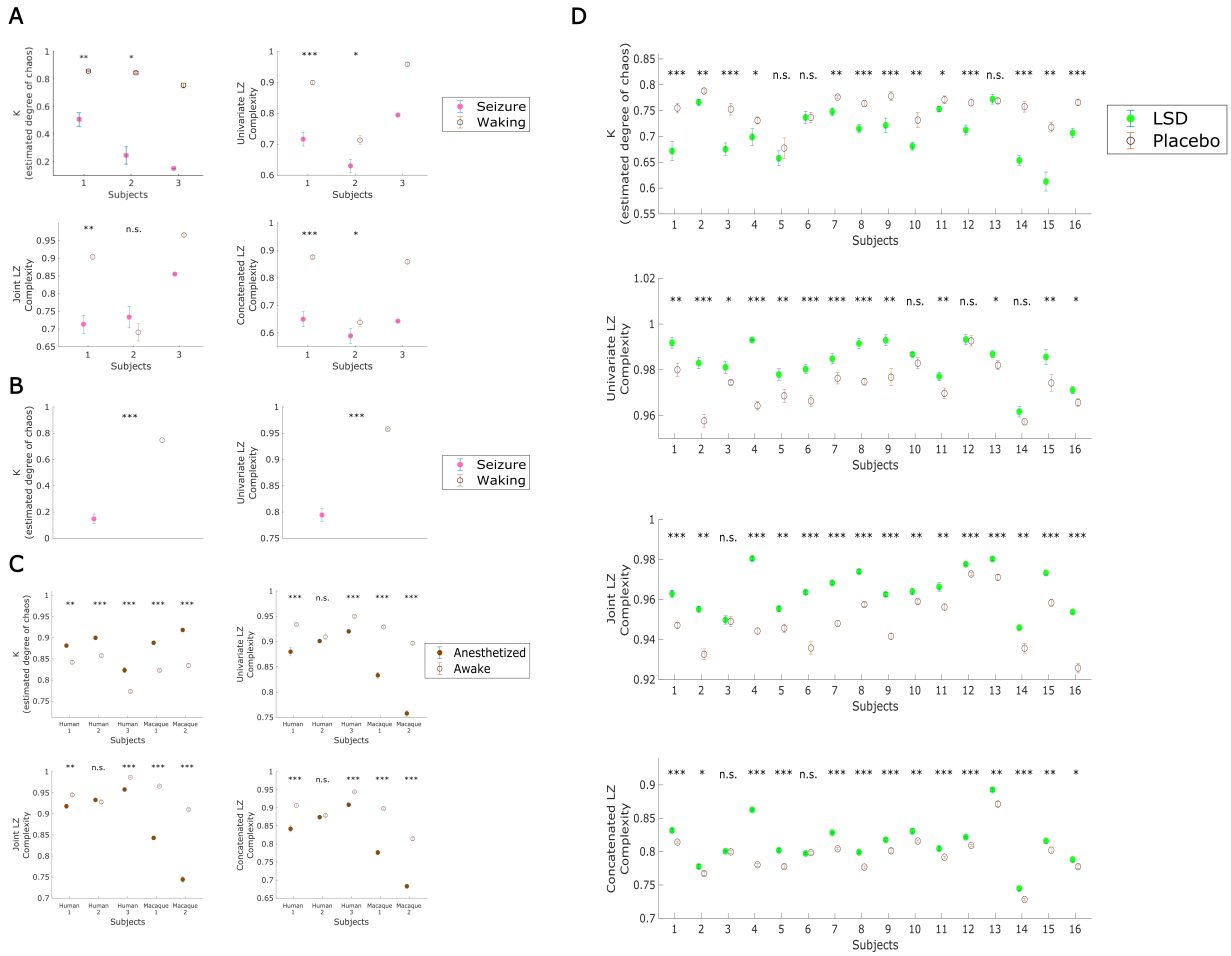
Fig. S5: (Caption on the following page.)

Fig. S5: **A**. We applied the modified 0-1 chaos test and three variants of Lempel-Ziv complexity to surface ECoG recordings from two human epilepsy patients (subjects 1 2) and to magnetoencephalography (MEG) recordings from another human epilepsy patient (subject 3) experiencing generalized seizures. Circles indicate the median estimated values across all trials per condition for a single subject, and errorbars indicate standard error of the median (estimated by taking the standard deviation of a bootstrap distribution of sample medians). Differences between conditions were tested using a left-tailed overlapping block bootstrap test (which controls for the non-independence of successive datapoints by preserving local time-series autocorrelations) with a block size of three trials (30 seconds of recording), to test against the null hypothesis that there is no decrease in the median K-statistic or Lempel-Ziv complexity during generalized seizures. The decreased chaoticity during generalized seizures was significant for both Subjects 1 and 2. Note that Subject 3 had only one $\sim$10 second generalized seizure during the duration of the recording, and so statistical comparison across trials was not possible - see **B** for statistical analysis of Subject 3's seizure on the level of individual MEG channels, rather than trials. Median information-richness, as measured by three different variants of Lempel-Ziv complexity, dropped significantly during generalized seizures for Seizure Subjects 1 and 2, with the exception of joint Lempel-Ziv complexity for Subject 2. Note again that no statistical analysis was performed for Seizure Subject 3 because the subject had only one generalized seizure; see **B** for analysis of the univariate Lempel-Ziv complexity of their individual channels across brain states. **B**. Here, we show the median and standard error of the median chaoticity (left) and univariate Lempel-Ziv complexity (right) across all channels during seizure subject 3's seizure trial and across their nine waking baseline trials. As was the case for the cross-trial comparisons (**A**), cross-channel differences between conditions were tested using left-tailed overlapping block bootstrap tests. The drop in the estimated chaoticity and information-richness of this subject's cortical electrodynamics was significant, consistent with the hypothesis that the dynamics of generalized seizures are information-poor and periodic/stable. **C**. We applied the modified 0-1 chaos test and the three variants of Lempel-Ziv complexity to surface ECoG recordings from three human subjects and two macaques under GABAergic anesthesia. Circles indicate the median values across all trials, per condition, and errorbars indicate standard error of the median. Differences in chaoticity between conditions were tested using a right-tailed overlapping block bootstrap test, to test against the null hypothesis of no increase in the median K-statistic under GABAergic anesthesia, and differences in information-richness were assessed using a left-tailed overlapping block bootstrap test, to specifically test against the null hypothesis that there is no decrease in Lempel-Ziv complexity during GABAergic anesthesia. The increased chaoticity under GABAergic anesthesia was significant for all subjects; the decrease in all measures of Lempel-Ziv complexity during anesthesia was significant for all subjects except Human Anesthesia Subject 2. **D**. We applied the modified 0-1 chaos test and Lempel-Ziv complexity algorithm to cortical MEG recordings from 16 human subjects following intravenous administration of either 75 μg of LSD or a saline placebo. Differences in chaoticity between conditions were tested using left-tailed overlapping block bootstrap tests, to test against the null hypothesis of no decrease in the median K-statistic during the psychedelic state relative to placebo, and differences in information-richness were assessed using a right-tailed overlapping block bootstrap test, to test against the null hypothesis of no increase in Lempel-Ziv complexity during the psychedelic state. The decreased chaoticity during the psychedelic state was significant for 13/16 subjects, univariate Lempel-Ziv complexity increased significantly for 15/16 subjects, joint Lempel-Ziv complexity increased significantly for 15/16 subjects, and concatenated Lempel-Ziv complexity increased significantly for 14/16 subjects. $*$ p<0.05, $**$ p<0.01, $***$ p<0.001.
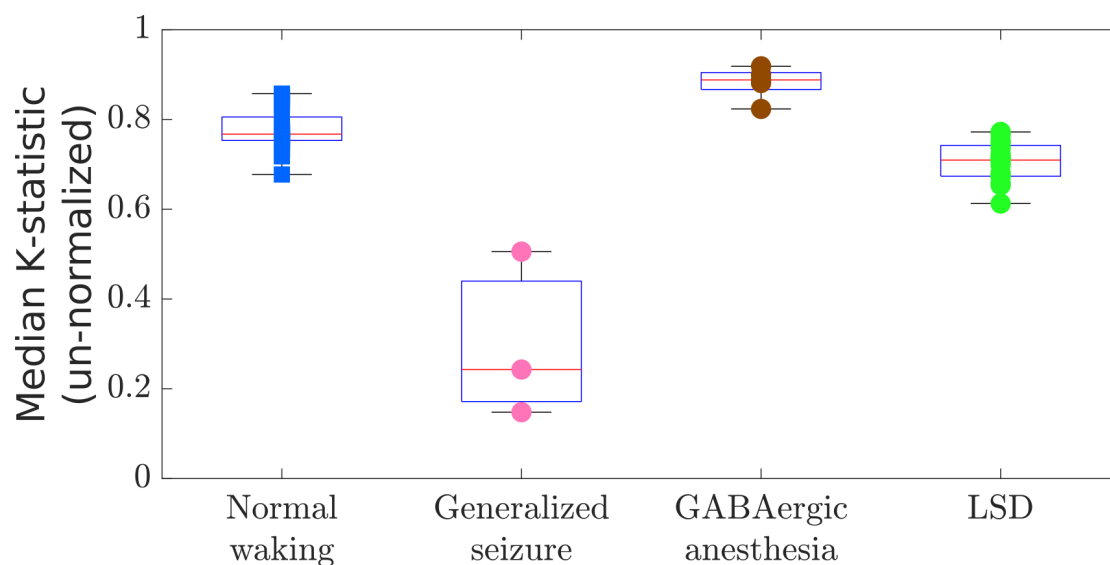
Fig. S6: We here display the un-normalized chaoticity estimates (K-statistic) for each subject in each brain state. There was little overlap across conditions, with the exception of partial overlap between normal waking and LSD states, which is unsurprising given that slow cortical electrodynamics are predicted to be near-critical in both states, with LSD tuning cortical dynamics slightly closer to edge-of-chaos criticality. Despite this partial overlap, un-normalized chaoticity estimates were significantly lower in the LSD state than they were both across all subjects' normal waking states (p=8.35e-05, right-tailed Wilcoxon rank-sum test, Bonferroni-corrected) and across the 16 LSD subjects' placebo state (p=0.0024, right-tailed Wilcoxon rank-sum test, Bonferroni-corrected). See Table S2 for an ANCOVA analysis of these un-normalized chaoticity estimates across brain states.
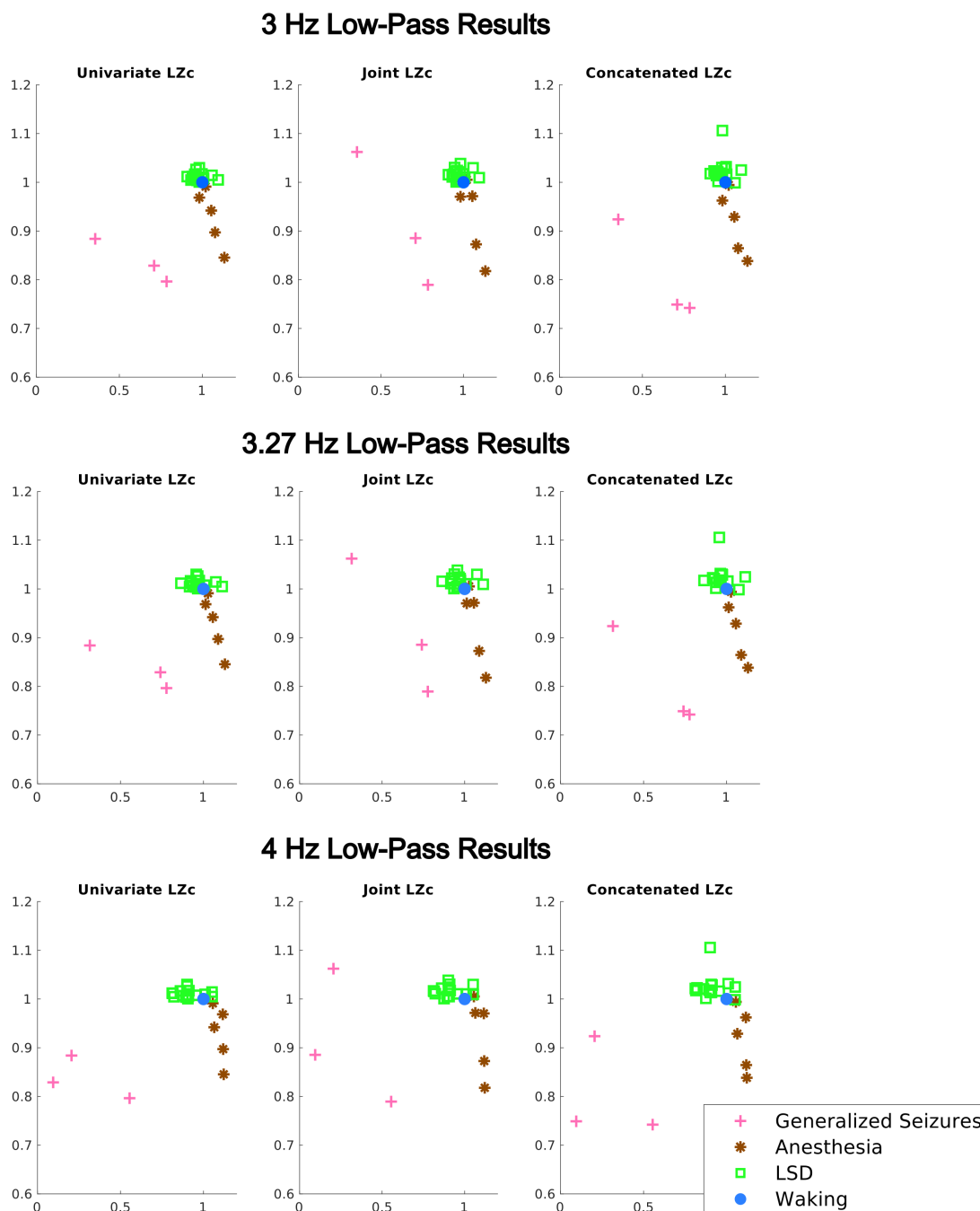
Fig. S7: We here repeated our analysis in Figure 3A, using a fixed frequency cutoff to low-pass filter all signals across all species, brain states, and data sets, rather than using the FOOOF algorithm to identify channel-specific oscillation frequencies. Because we are interested in low-frequency oscillations, we set the fixed frequency cutoffs to 3 Hz and 4 Hz, which are variably used as the upper limit of slow/delta oscillations, as well 3.27 Hz, which was the mean frequency cutoff selected by the FOOOF algorithm across all datasets. While using fixed frequency cutoffs preserved the general inverse-U shape between chaoticity estimates and the information-richness of cortical electrodynamics (normalized to each subject's own normal waking baseline), there was greater variability within specific brain states. Note that all channels were included in this analysis.
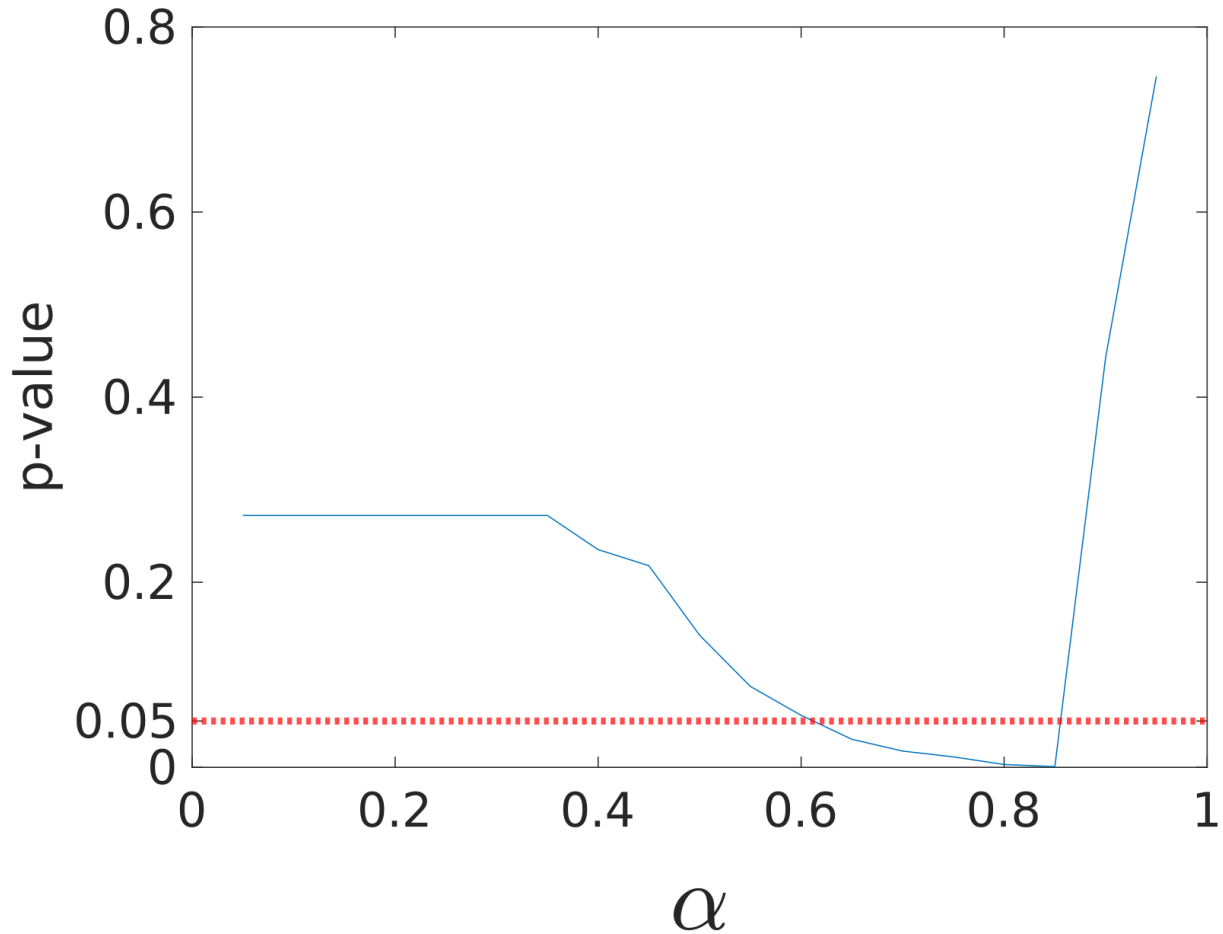
Fig. S8: Our new time-series estimate c of proximity to edge-of-chaos criticality, based on a nonlinear transformation of the K-statistic outputted by the modified 0-1 chaos test, includes a parameter α, which must be set between zero and one (see Materials and Methods). To explore the optimal range of α values for which c might be useful as a clinical index of consciousness, we converted the cross-trial, state-specific medians of chaoticity estimates (un-normalized K-statistics) of 12 subjects for whom data were available from both conscious and unconscious states (namely five anesthesia subjects, three generalized seizure subjects, and four DOC patients) into our criticality measure c, using 19 unique values of α. For each value of α, we performed a right-tailed Wilcoxon rank sum test between the 12 values of c from conscious states and the 12 values of c from unconscious states, to test against the null hypothesis that there is no increase in median estimates of criticality during conscious states. We here plot the uncorrected p-values of these tests, for each value of α assessed. After conservative Bonferroni correction, the difference in c at α=0.85 between conscious and unconscious states remained significant, suggesting that α should be set around this value when exploring the potential utility of our new criticality measure c as a potential correlate of conscious level. We therefore set α to 0.85 in all subsequent analyses using our measure c in both the main body of the paper and SI Appendix.
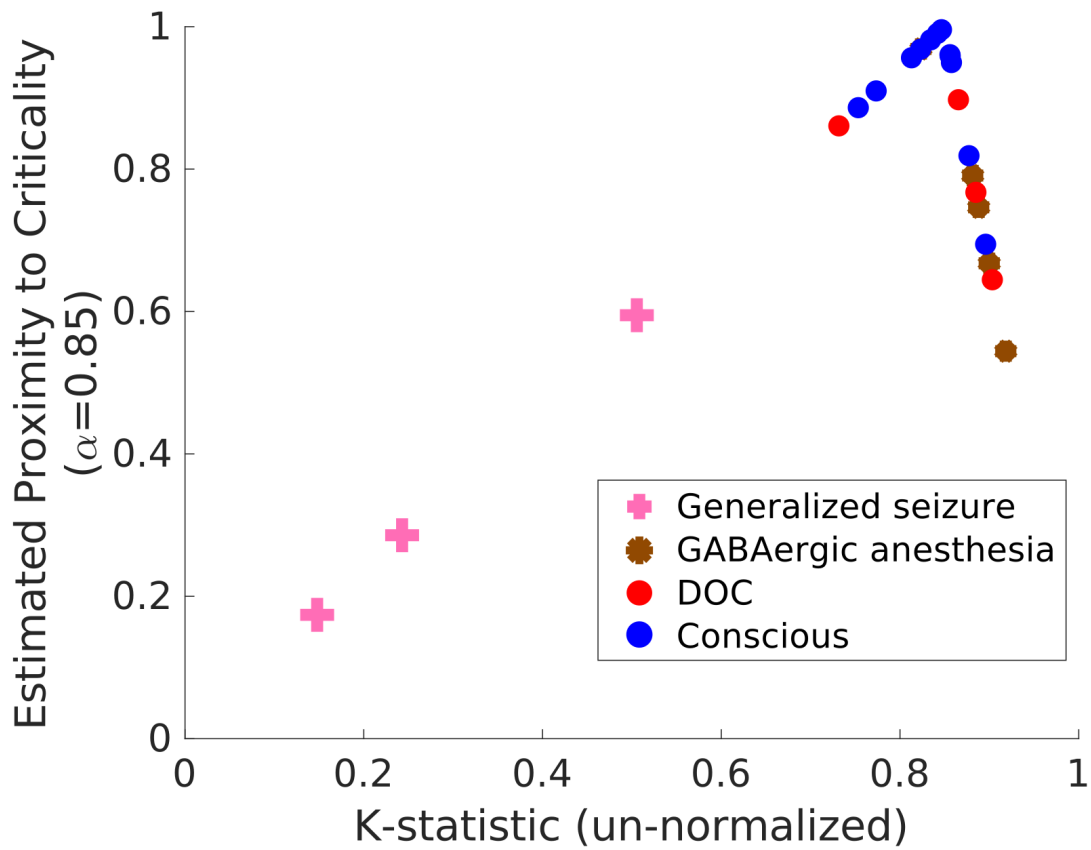
Fig. S9: We here plot all estimated criticality values from Figure 4 against the raw K-statistic values from which those criticality estimates were derived. Note that, by design, our criticality estimate peaks at whatever value α is set to, which here is 0.85, based on our analysis in Fig. S8.
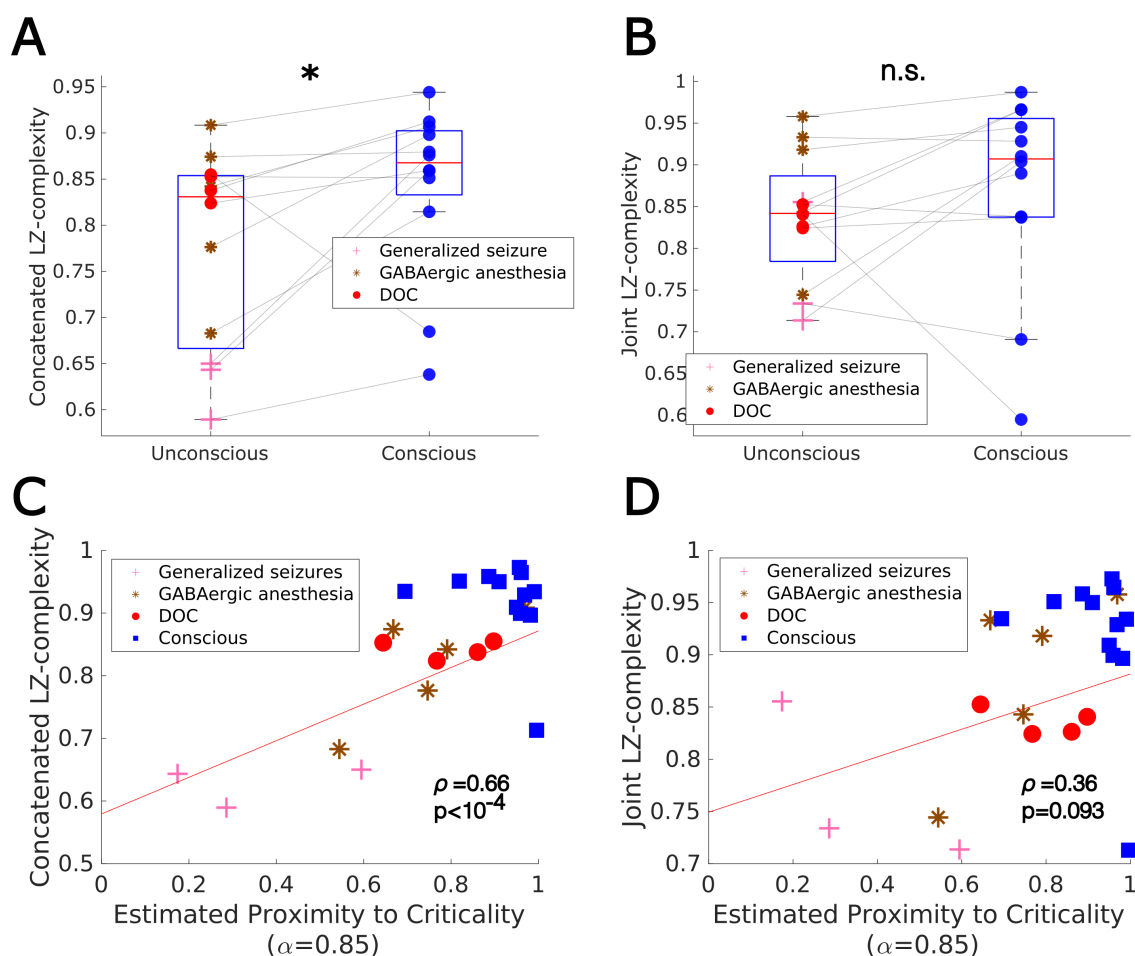
Fig. S10: **A** As was the case for univariate Lempel-Ziv complexity (Fig. 4B), concatenated Lempel-Ziv was significantly higher during conscious states than during unconscious states for the 12 subjects for whom data were available from both conscious and unconscious states (five anesthesia subjects, three generalized seizure subjects, and four DOC patients). Each dot represents the cross-trial median across a single subject's trials in either their unconscious or conscious state. Significance was assessed across subjects using a right-tailed Wilcoxon rank-sum test. **B** A cross-subject right-tailed Wilcoxon rank-sum test did not reveal a significant difference in joint Lempel-Ziv complexity across conscious vs. unconscious states. **C** As was the case for univariate Lempel-Ziv complexity (Fig. 4C), concatenated Lempel-Ziv complexity was significantly correlated with our criticality measure c at α=0.85 across subjects and states (partial correlation ρ=0.66, p< 10^{-4} , controlling for median frequency at which signals were low-pass filtered). **D** Joint Lempel-Ziv complexity was not significantly correlated with our criticality measure.
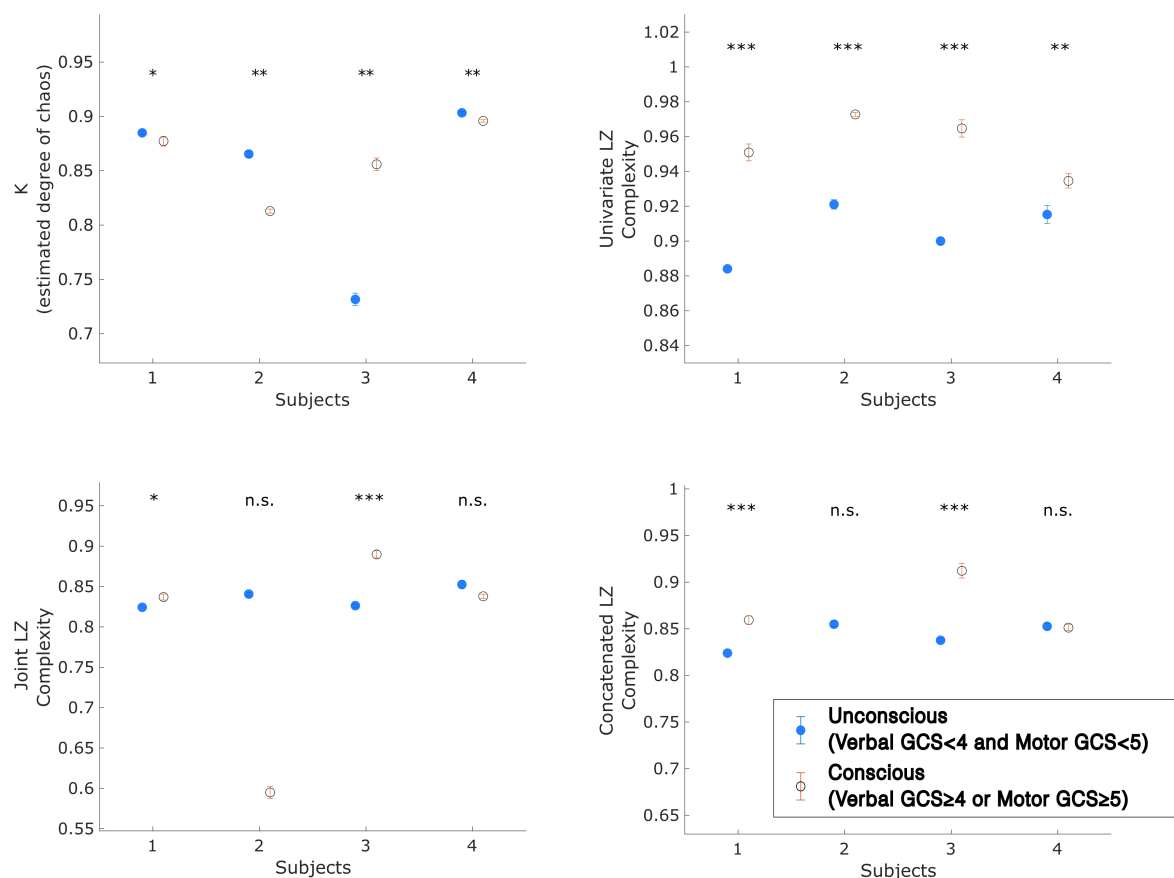
Fig. S11: We applied the modified 0-1 chaos test and the three variants of Lempel-Ziv complexity to clinical EEG recordings of the cortical electrodynamics of four human patients who recovered consciousness after going into a coma, following a traumatic brain injury. Circles indicate the median estimated chaoticity across all trials, per condition, and errorbars indicate standard error of the median. Differences in estimated chaoticity between conditions were tested using a two-tailed overlapping block bootstrap test (the test was two-tailed, rather than one-tailed, because we had no *a priori* prediction as to whether chaoticity would increase or decrease during unconscious relative to conscious states). Differences in information-richness were assessed using a left-tailed overlapping block bootstrap test, to specifically test against the null hypothesis that there is no decrease in Lempel-Ziv complexity in DOC. We found that estimated chaoticity (top left) was significantly higher in unconscious than conscious states for three out of four of the patients, similar to what we observed for GABAergic anesthesia (SI Appendix, Fig. S5C), but was significantly lower in the fourth patient, similar to what we observed for generalized seizures (SI Appendix, Fig. 5A-B). Univariate Lempel-Ziv complexity (top right) was significantly lower during unconscious than conscious states for all patients, recapitulating what we observed for both anesthesia and generalized seizures (SI Appendix, Fig. S5), while results with both measures of multivariate Lempel-Ziv complexity were inconsistent across patients (bottom).
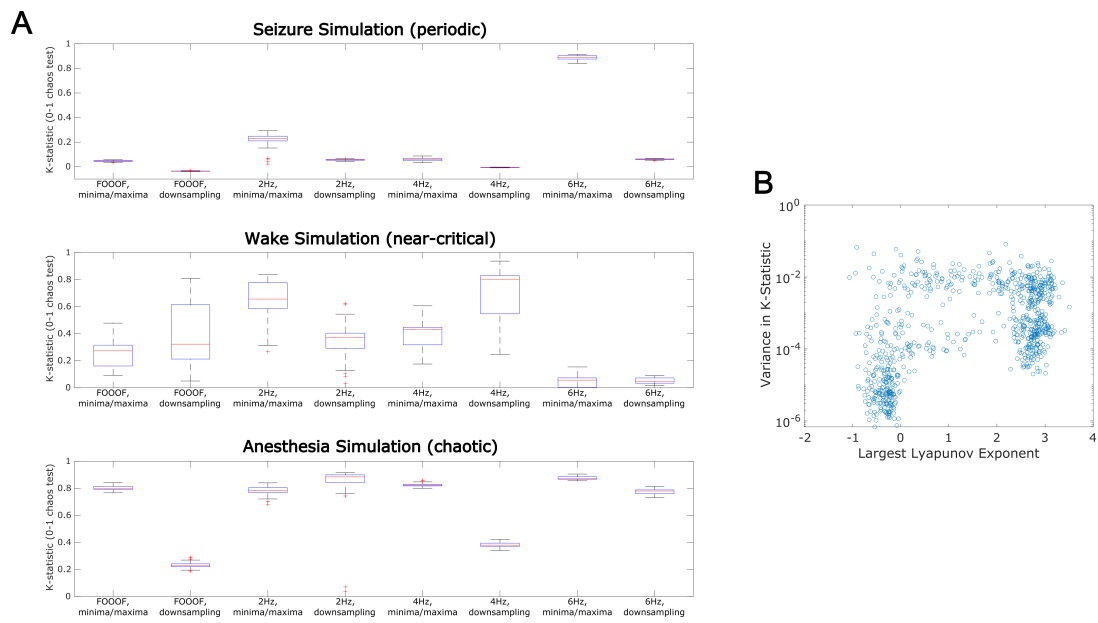
Fig. S12: (Caption on the following page.)

Fig. S12: **A**. To ensure that our processing pipeline produces estimates of chaoticity that are both accurate and stable, we ran 100 simulations of the mean-field model in its seizure (periodic), waking (near-critical), and anesthetized (chaotic) states. Each simulation included unique noise inputs. Thus, the deterministic component of all 100 simulations in a given state had the same ground-truth largest Lyapunov exponent (i.e. level of chaoticity), but the actual time-series produced in each simulation would be unique, due to the unique noise inputs. As in Table S6, we compared results using four low-pass filtering methods (namely, where the low-pass filter frequency was determined either by the FOOOF algorithm or set at 2, 4, or 6 Hz) and two different methods for time-discretization (namely, downsampling or taking the local minima and maxima) of the low-pass filtered signal. Results were generally stable in both the seizure (periodic) and anesthesia (chaotic) states. Though results were less stable for the waking (near-critical) state, they were comparably stable (compared to other methods) when taking the local minima and maxima of a time-series that was low-pass filtered at a frequency determined using the FOOOF algorithm. Importantly, this method also produced the most accurate chaoticity estimates (Tables S6-S7). Thus, given both the accuracy and relative stability of chaoticity estimates using this method, the chaoticity of all empirical time-series in this paper was estimated using the local minima and maxima of signals low-pass filtered using the FOOOF algorithm. **B**. To assess whether there was any systematic relationship between the stability of chaoticity estimates using this method and ground-truth chaoticity, we ran 10 simulations of each of the 776 parameter configurations of the mean-field model assessed in this paper. (Note that we ran 10 rather than 100 simulations, as in **A**, because of the long computation times involved). For each run, we estimated the chaoticity of the simulated time-series using the local minima and maxima of signals low-pass filtered using the FOOOF algorithm, and calculated the variance of the median K-statistic across those 10 runs for each parameter configuration. Because variance was low for all parameter configurations, we plotted the results on a log-scale, which revealed a slight but consistent increase in the variance of the K-statistic near criticality.
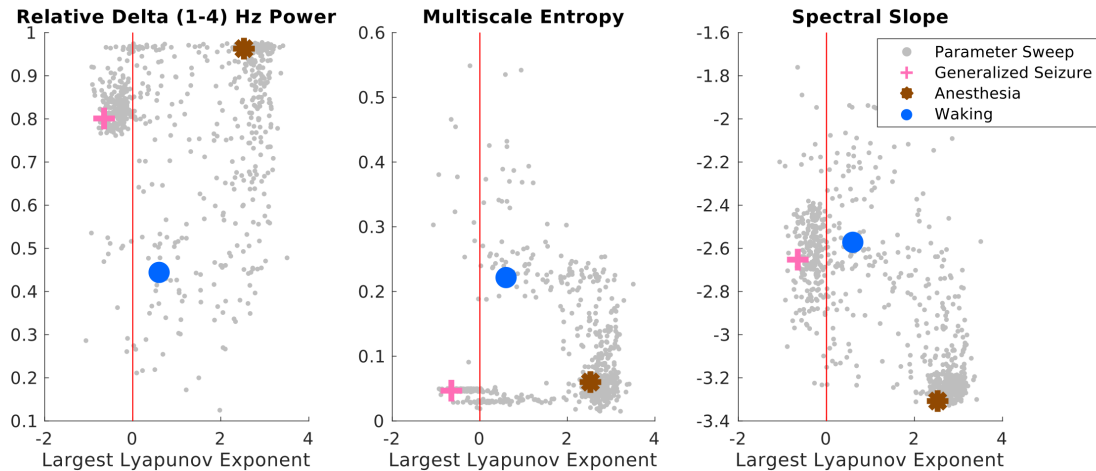
Fig. S13: We here plot the behavior of three previously validated correlates of anesthetic depth: 1) relative delta power[12, 13], here calculated as total power between 1 and 4 Hz divided by total power between 1 and 45 Hz, 2) multiscale sample entropy[14], using the parameters described in Costa et al[15], which have been shown to robustly track sevoflurane effect site concentration[14] (namely, segment length m=2, tolerance r=0.15, and time scale τ=1), and 3) spectral slope[16, 17] (using the automated spectral slope calculation of the FOOOF algorithm[11]). Although prior analyses of spectral slope during anesthesia assessed slope between 30 and 45 or 50 Hz, the mean-field model analyzed here only explicitly simulates low-frequency dynamics, and so we assessed spectral slope from 0.1 to 45 Hz. Consistent with prior empirical work, we found a clear rise in relative delta power, reduction of multiscale entropy, and steepening of spectral slope in the chaotic phase of the model more generally, and in the simulated anesthesia state more specifically. Moreover, we found that, like Lempel-Ziv complexity (Fig. 2), multiscale entropy displayed its highest values near the edge-of-chaos critical point, with reductions in both the periodic and chaotic phases.
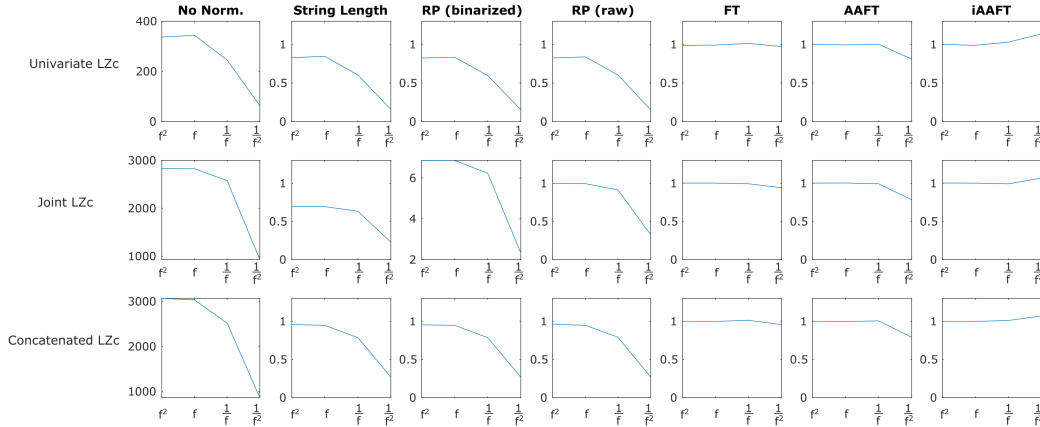
Fig. S14: In order to compare the amount of non-redundant information in different signals, Lempel-Ziv complexity is typically normalized to lie roughly between 0 and 1. We here test several different normalization approaches by applying them to noise signals with different spectral slopes; this is important in comparing Lempel-Ziv complexity across different brain states, as the spectral profiles of brain signals can vary significantly across different brain states. The x-axes here refer to multivariate noise signals with increasingly negative spectral slopes: f^2 (violet) noise, f (blue) noise, $1/f$ (pink) noise, and $1/f^2$ (red) noise. All of these signals are entirely random (and thus contain entirely non-redundant information), and vary only by their spectral properties; thus, a properly normalized measure of Lempel-Ziv complexity should be constant (and approaching the ceiling of 1) for each of these random processes. The first column ("No Norm.") shows the behavior of our three measures of Lempel-Ziv complexity as a function of the spectral profile of the noise signals; note the drop as the power spectrum steepens from pink ($1/f$) noise to red ($1/f^2$) noise. The second column, "String Length," shows the behavior of the three complexity measures normalized by $T/\log_2 T$, where T is the length of the binary string being compressed; note that this form of normalized Lempel-Ziv complexity likewise varies as a function of the spectral slope of the random signals. The third column, "RP (binarized)," shows the alternative normalization scheme used by Schartner and colleagues[18, 19], which divides the Lempel-Ziv complexity of a signal (after it has been binarized) by the Lempel-Ziv complexity of a random shuffle of the binarized form of the signal; this likewise is affected by spectral slope. The fourth column, "RP (raw)" is similar, but instead divides the Lempel-Ziv complexity of a signal by the Lempel-Ziv complexity of a random shuffle of that continuous signal (i.e., Lempel-Ziv complexity is calculated for a binarized version of the original signal, and for a binarized version of the shuffled signal, and the former is normalized by the latter). The final three columns show the behavior of Lempel-Ziv complexity of a signal divided by the Lempel-Ziv complexity of a phase-randomized surrogate of that signal, following the methodology of Brito and colleagues[20]. A phase-randomized surrogate preserves the spectral properties of the original signal but is otherwise random. We used three phase-randomized surrogate algorithms: Fourier transform surrogates ("FT"), amplitude adjusted Fourier transform surrogates ("AAFT") and iterative amplitude adjusted Fourier transform surrogates ("iAAFT"). Normalizing by the Lempel-Ziv complexity of surrogates generated by any of these three algorithms produced desirable behavior - namely, a consistent normalization to near one for any noise signal, regardless of its spectral properties - but the least variance as a function of spectral slope was produced by Fourier transform surrogates ("FT"), and so we used this algorithm throughout the rest of this paper to create surrogates by which to normalize Lempel-Ziv complexity.

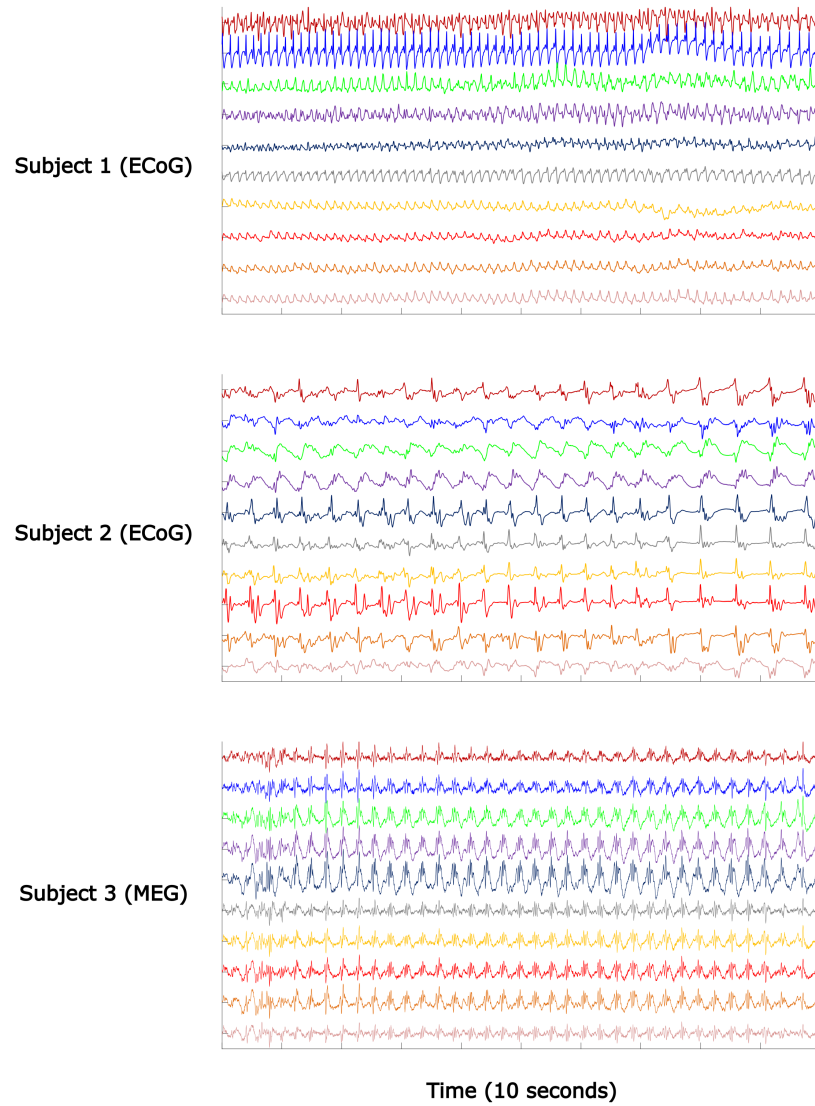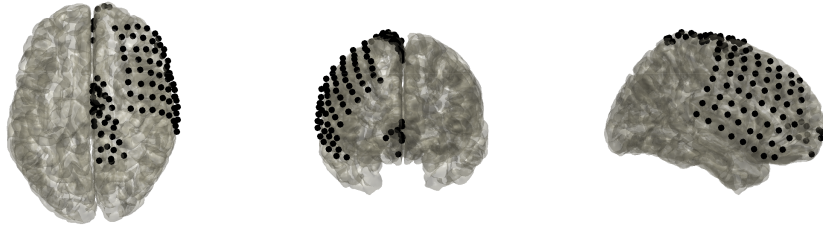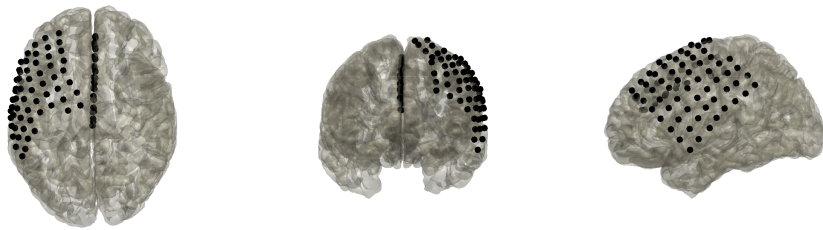Fig. S15: 10-second time-traces from 10 sample channels during generalized seizures from our three seizure subjects. The subject numbers match those in Figs. S2-S4.

Human Anesthesia Subject 1

Human Anesthesia Subject 2
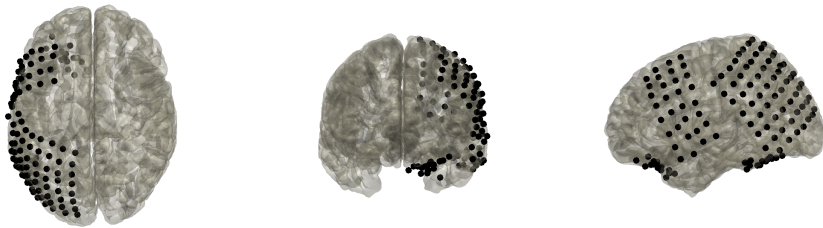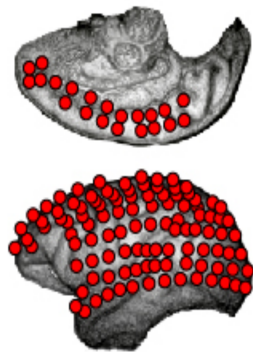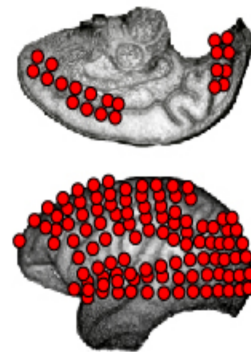
Human Anesthesia Subject 3

Macaque Anesthesia
Subject 1

Macaque Anesthesia
Subject 2

Fig. S16: Surface electrocorticography (ECoG) electrode placement for our anesthesia subjects.

SUPPLEMENTARY TABLES

Table S1: As described in the main body of the paper, we did not estimate chaoticity from any channel, in a given trial, for which the FOOOF algorithm failed to identify an oscillatory peak within the 1-6 Hz range. We here enumerate the (rounded) percentage of channels(x)trials that were thus *ex*cluded from our chaoticity analysis. Note that, in general, only a minority of channels were thus excluded, and that there were no clear differences in the number of excluded channels in different brain states (which we confirm statistically in Tables S2-S3)

	Percentage of channels(x)trials excluded from chaos analysis	
Subject	Normal waking	Altered state
Anesthesia Subject 1 (ECoG, human)	9%	14%
Anesthesia Subject 2 (ECoG, human)	18%	21%
Anesthesia Subject 3 (ECoG, human)	14%	16%
Anesthesia Subject 4 (ECoG, macaque)	10%	11%
Anesthesia Subject 5 (ECoG, macaque)	7%	18%
Seizure Subject 1 (ECoG, human)	23%	21%
Seizure Subject 2 (ECoG, human)	9%	1%
Seizure Subject 3 (MEG, human)	22%	0%
LSD Subject 1 (MEG, human)	29%	32%
LSD Subject 2 (MEG, human)	14%	20%
LSD Subject 3 (MEG, human)	21%	25%
LSD Subject 4 (MEG, human)	31%	27%
LSD Subject 5 (MEG, human)	7%	11%
LSD Subject 6 (MEG, human)	24%	25%
LSD Subject 7 (MEG, human)	13%	13%
LSD Subject 8 (MEG, human)	23%	28%
LSD Subject 9 (MEG, human)	27%	27%
LSD Subject 10 (MEG, human)	26%	32%
LSD Subject 11 (MEG, human)	23%	22%
LSD Subject 12 (MEG, human)	22%	30%
LSD Subject 13 (MEG, human)	15%	17%
LSD Subject 14 (MEG, human)	28%	28%
LSD Subject 15 (MEG, human)	18%	14%
LSD Subject 16 (MEG, human)	23%	31%
DOC patient 1 (EEG, human)	1%	0%
DOC patient 2 (EEG, human)	18%	32%
DOC patient 3 (EEG, human)	35%	27%
DOC patient 4 (EEG, human)	23%	21%

Table S2: We tested whether observed differences in estimated chaoticity across brain states were potentially driven by the frequency at which signals were low-pass filtered, and/or the relative spectral power of activity beneath that frequency cutoff (calculated as total power under the low-pass filter frequency divided by total spectral power under 45 Hz), and/or the number of channels that were excluded from chaoticity estimates (owing to the failure of the FOOOF algorithm to identify an oscillation in the 1-6 Hz range in those channels - see Materials and Methods). To do so, we used a permutation-based nonparametric ANCOVA with 1,000 permutations, following the method described by Petraitis and colleagues[21]. We set the median K-statistic as the response variable, brain state (i.e. normal waking, generalized seizure, anesthesia, or LSD) as the group label, and set the covariates to 1) the median frequency at which signals were low-pass filtered, 2) the median relative spectral power beneath that frequency, and 3) the percentage of channels that were excluded from each subject's chaoticity estimates. We found that only brain state significantly explained the observed variance across subjects in the estimated chaoticity of slow cortical electrodynamics, with no significant effect of the covariates or their interactions with brain state.

Variable	F-statistic	p-value
Brain State	43.477	0.001
Slow frequency cutoff	0.512	0.475
Slow frequency power	0.074	0.786
Percent channels excluded	0.574	0.444
Brain state*slow frequency cutoff	0	1
Brain state*slow frequency power	0.479	0.492
Brain state*percent channels excluded	0.893	0.369
Brain state*all covariates	0.382	0.542

Table S3: We repeated our nonparametric, permutation-based ANCOVA from Table S1, using K-statistic values normalized to each subject's normal waking baseline (as reported in Figure 3A) rather than raw K-statistic values. We again found that only brain state significantly explained the observed variance in the estimated chaoticity of slow cortical electrodynamics, with no significant effect of either the covariates or their interactions with brain state, though percentage of excluded channels bordered on significance as a covariate.

Variable	F-statistic	p-value
Brain State	90.644	0.001
Slow frequency cutoff	2.817	0.076
Slow frequency power	0.007	0.946
Percent channels excluded	4.316	0.05
Brain state*slow frequency cutoff	0	1
Brain state*slow frequency power	0.023	0.912
Brain state*percent channels excluded	0.252	0.710
Brain state*all covariates	0.027	0.911

Table S4: We previously described[3] a test to determine whether a signal is generated by a predominantly deterministic system (linear or nonlinear). The test compares the permutation entropy of a signal to the permutation entropies of 1,000 amplitude adjusted Fourier transform surrogates and 1,000 cyclic phase permutation surrogates of that signal. If the permutation entropy of the original signal falls within either surrogate distribution, then the signal is classified as predominantly or "operationally" stochastic. We identified a failure case of this method, which is that for short, noise-free signals sampled at a high frequency from deterministic, continuous-time systems, the cyclic phase permutation algorithm generates surrogates with identical permutation entropies. This in turn can lead to misclassifications of deterministic processes as stochastic. We here modify our original test to catch this edge case: if the cyclic phase permutation algorithm fails to generate surrogates with at least 500 unique permutation entropy values, then jitter in the form of 2.5% white noise is incrementally added to the original signal until this failure case is broken. We here tested the accuracy of both our original and modified test on a broad range of dynamical systems, the code for which is included alongside our previously described Chaos Decision Tree Algorithm (see our prior work for model equations and parameters[3]). Note that SNA stands for "strange nonchaotic attractor." We excluded one system described in our previous work, namely the noise-driven sine map, because it is unclear whether its dynamics are in fact predomoninantly stochastic, or whether they are better characterized as noise-induced tunneling between quasi-stable, deterministic attractor states[3]. We also applied both our original and modified stochasticity test to all 120 nodes of the mean-field model studied here, with its noise inputs turned off (so its dynamics are fully deterministic), in its seizure, waking, and anesthesia states. We found that our modified stochasticity test performed as well as the original test for all systems described in our previous work, and markedly outperformed the original test for the mean-field simulations of low-frequency cortical activity. We therefore applied this modified test to our real cortical recordings (Table S5). Table on next page.

	Original Stochasticity Test Accuracy	Modified Stochasticity Test Accuracy
ARMA process (linear stochastic)	67/100 (67%)	71/100 (71%)
Bounded random walk (nonlinear stochastic)	100/100 (100%)	100/100 (100%)
Cubic Map (chaotic)	100/100 (100%)	100/100 (100%)
Cubic Map (Heagey-Hammel SNA)	100/100 (100%)	100/100 (100%)
Cubic Map (periodic-doubled)	100/100 (100%)	100/100 (100%)
Cubic Map (periodic)	100/100 (100%)	100/100 (100%)
Cubic Map (type-3 intermittency SNA)	100/100 (100%)	100/100 (100%)
Cyclostationary process (linear stochastic)	98/100 (98%)	98/100 (98%)
Freitas map (nonlinear stochastic)	99/100 (99%)	99/100 (99%)
Generalized Hénon Map (hyperchaotic)	100/100 (100%)	100/100 (100%)
GOPY map (SNA)	100/100 (100%)	100/100 (100%)
Granulocyte levels (chaotic)	100/100 (100%)	100/100 (100%)
Granulocyte levels (periodic)	100/100 (100%)	100/100 (100%)
Hénon map (periodic)	100/100 (100%)	100/100 (100%)
Ikeda map (chaotic)	100/100 (100%)	100/100 (100%)
Logistic map (chaotic)	100/100 (100%)	100/100 (100%)
Logistic map (periodic)	100/100 (100%)	100/100 (100%)
Lorenz system (chaotic)	100/100 (100%)	100/100 (100%)
Poincaré oscillator (chaotic)	100/100 (100%)	100/100 (100%)
Poincaré oscillator (periodic)	100/100 (100%)	100/100 (100%)
Poincaré oscillator (quasi-periodic)	100/100 (100%)	100/100 (100%)
Random walk (linear stochastic)	100/100 (100%)	100/100 (100%)
Rössler oscillator (chaotic)	100/100 (100%)	100/100 (100%)
Simulated anesthesia state (chaotic)	0/120 (0%)	117/120 (98%)
Simulated seizure (periodic)	0/120 (0%)	120/120 (100%)
Simulated waking state (chaotic, near-critical)	1/120 (1%)	98/120 (82%)
Spiking Izhikevich neuron (chaotic)	100/100 (100%)	100/100 (100%)
Trended random walk (linear stochastic)	100/100 (100%)	99/100 (99%)
Unfiltered blue noise (linear stochastic)	100/100 (100%)	100/100 (100%)
Unfiltered pink noise (linear stochastic)	100/100 (100%)	100/100 (100%)
Unfiltered red noise (linear stochastic)	100/100 (100%)	100/100 (100%)
Unfiltered violet noise (linear stochastic)	100/100 (100%)	100/100 (100%)
Unfiltered white noise (linear stochastic)	100/100 (100%)	100/100 (100%)

Table S5: To test whether low-frequency cortical electrodynamics are predominantly deterministic (which is an important assumption of the 0-1 chaos test), as well as to test against the possibility that our results were potentially driven by changing levels of stochasticity in low-frequency cortical dynamics rather than by changing levels of chaoticity, we applied the modified test of signal stochasticity described in Table S4 to all of our empirical datasets. Specifically, we applied the test to all data (channels x trials) low-pass filtered using the FOOOF algorithm (i.e., the data for which we assessed low-frequency chaoticity using the 0-1 test). We found that low-frequency dynamics from a majority (75%) of channels(x)trials were classified as predominantly deterministic. Moreover, a cross-subject, two-tailed Wilcoxon rank-sum test comparing percentage of channels(x)trials classified as stochastic in normal waking versus altered states revealed no significant difference between conditions (p=0.2446). Additionally, there was no correlation between the change in each subject's median K-statistic across conditions and the change in the percentage of their channels(x)trials that were classified as stochastic (Pearson correlation r=-0.304, p=0.116; partial correlation ρ=-0.189, p=0.346, controlling for change in median frequency at which signals were low-pass filtered). To further test against the possibility that these findings were potentially driven by our low-pass filtering method, we generated 100 simulations of 5,000 time-points of violet, blue, white, pink, and red noise, and applied this stochasticity test to these simulated noise samples after low-pass filtering in the 1-6 Hz range using the FOOOF algorithm (note that, as was the case for the empirical data, a simulated noise signal was excluded if the FOOOF algorithm did not identify an oscillation in this frequency range). Although our stochasticity test performed with perfect accuracy in classifying unfiltered noise as stochastic (Table S4), performance did drop for low-pass filtered noise. That said, we note that performance was very high for both filtered pink and red noise, whose power spectra ($\frac{1}{f}$ and $\frac{1}{f^2}$, respectively) more closely match that of real neural electrodynamics[11] than do those of other noise colors. Taken together, these results suggest that low-frequency cortical electrodynamics are predominantly deterministic, and that observed changes in the K-statistic across brain states result from changing levels of chaoticity in those electrodynamics, as predicted, rather than changing levels of stochasticity. Table on next page.

Subject	Fraction of channels(x)trials classified as stochastic (low-frequency)	
	Normal waking	Altered state
Anesthesia Subject 1 (ECoG, human)	3770/5421 (70%)	5499/6522 (84%)
Anesthesia Subject 2 (ECoG, human)	8538/11178 (76%)	9121/10853 (84%)
Anesthesia Subject 3 (ECoG, human)	5070/10041 (50%)	4423/8030 (55%)
Anesthesia Subject 4 (ECoG, macaque)	264/11948 (2%)	0/13528 (0%)
Anesthesia Subject 5 (ECoG, macaque)	226/11772 (2%)	4/10249 (0%)
Seizure Subject 1 (ECoG, human)	9/1539 (1%)	0/225 (0%)
Seizure Subject 2 (ECoG, human)	0/1385 (0%)	0/1128 (0%)
Seizure Subject 3 (MEG, human)	208/1007 (21%)	54/143 (38%)
LSD Subject 1 (MEG, human)	2245/8677 (26%)	1445/9870 (15%)
LSD Subject 2 (MEG, human)	2689/10081 (27%)	768/6548 (12%)
LSD Subject 3 (MEG, human)	2616/12679 (21%)	2128/12017 (18%)
LSD Subject 4 (MEG, human)	2674/13300 (20%)	1036/13732 (8%)
LSD Subject 5 (MEG, human)	1644/6265 (26%)	2226/6343 (35%)
LSD Subject 6 (MEG, human)	1854/7448 (25%)	1230/10564 (12%)
LSD Subject 7 (MEG, human)	2532/10526 (24%)	1843/10549 (17%)
LSD Subject 8 (MEG, human)	2658/10412 (26%)	2236/9667 (23%)
LSD Subject 9 (MEG, human)	795/3193 (25%)	558/2824 (20%)
LSD Subject 10 (MEG, human)	486/6344 (8%)	376/5946 (6%)
LSD Subject 11 (MEG, human)	3118/12201 (26%)	3059/13317 (23%)
LSD Subject 12 (MEG, human)	1545/8818 (18%)	1406/8866 (16%)
LSD Subject 13 (MEG, human)	63/1018 (6%)	54/939 (6%)
LSD Subject 14 (MEG, human)	1964/8765 (22%)	1432/7688 (19%)
LSD Subject 15 (MEG, human)	2806/9350 (30%)	1438/10028 (14%)
LSD Subject 16 (MEG, human)	1310/7855 (17%)	1132/6439 (18%)
DOC patient 1 (EEG, human)	360/3230 (11%)	1481/11914 (12%)
DOC patient 2 (EEG, human)	6187/12138 (51%)	1643/3904 (42%)
DOC patient 3 (EEG, human)	221/416 (53%)	12538/28752 (44%)
DOC patient 4 (EEG, human)	1174/2565 (46%)	869/2199 (40%)
Filtered violet noise	82/83 (99%)	
Filtered blue noise	61/94 (65%)	
Filtered white noise	33/88 (38%)	
Filtered pink noise	65/93 (70%)	
Filtered red noise	91/92 (99%)	

Table S6: We here compare different time-series analysis methods for tracking changing levels of chaoticity in a system. To do so, we assessed the Pearson correlation r and associated p-values (Bonferroni-corrected) between the ground-truth largest Lyapunov exponent of the mean-field cortical model studied in this paper (calculated with the noise input turned off) and the K-statistic of the 0-1 chaos test, applied to the time-discretized, low-frequency component of the simulated dynamics of the model (with the noise input turned on, so as to better assess their ability to track changing chaoticity in real cortical dynamics). Low-frequency dynamics were extracted using EEGLAB's two-way least-squares FIR low-pass filtering, as described in the Materials and Methods. Cutoff frequencies for low-pass filtering were determined in a data-driven manner using the FOOOF algorithm, or were set at 2 Hz, 4 Hz, or 6 Hz. Once data were low-pass filtered, they were time-discretized using either the iterative downsampling method described in our prior work[3], or by taking all local minima and maxima of the simulated signals[22]. We further tested the ability of these analysis methods to track varying degrees of chaos in the presence of very high levels of either white or pink (1/f) measurement noise, where the noise amplitude equaled half (50%) the standard deviation of the underlying signal. Overall, we found that the K-statistic, when applied to low-frequency activity extracted using the FOOOF algorithm and discretized using the local minima/maxima method (bolded), outperformed all other methods in tracking the ground-truth chaoticity of the model, and was unaffected by even large amounts of measurement noise. This method also produced stable estimates of chaoticity across unique model simulations (Fig. S12). We therefore used this method to track changing levels of chaoticity in our real cortical recordings.

	Noise-free		50% White Noise		50% Pink (1/f) Noise	
	r	p-value	r	p-value	r	p-value
FOOOF, minima/maxima	**0.84**	**<10e-4**	**0.84**	**<10e-4**	**0.83**	**<10e-4**
FOOOF, downsampling	0.72	<10e-4	0.72	<10e-4	0.73	<10e-4
2 Hz, minima/maxima	0.75	<10e-4	0.72	<10e-4	0.38	<10e-4
2 Hz, downsampling	0.16	<10e-4	0.1	n.s.	0.06	n.s.
4 Hz, minima/maxima	0.74	<10e-4	0.74	<10e-4	0.75	<10e-4
4 Hz, downsampling	0.73	<10e-4	0.73	<10e-4	0.67	<10e-4
6 Hz, minima/maxima	-0.20	<10e-4	-0.22	<10e-4	-0.39	<10e-4
6 Hz, downsampling	0.73	<10e-4	0.72	<10e-4	0.47	<10e-4

Table S7: Because the FOOOF algorithm picks a unique frequency at which to low-pass filter data for each channel and trial, we here calculated the partial correlation ρ (and Bonferroni-corrected p-values) between the ground-truth largest Lyapunov exponents of the mean-field model and the K-statistic calculated using the FOOOF algorithm as described above, controlling for the low-pass filter frequency selected by the FOOOF algorithm. We found that even when controlling for the frequency selected by the FOOOF algorithm for low-pass filtering, the method identified in Table S6 as superior to all alternatives - namely, applying the 0-1 chaos test to the local minima and maxima of a signal low-pass filtered at a frequency identified by the FOOOF algorithm - robustly tracks ground-truth chaoticity. We moreover note that, unlike the minima/maxima time-discretization method, controlling for frequency markedly reduced the correlation between ground-truth largest Lyapunov exponents and the K-statistic calculated using the iterative down-sampling method.

	Noise-free		50% White Noise		50% Pink (1/f) Noise	
	ρ	p-value	ρ	p-value	ρ	p-value
FOOOF, minima/maxima	**0.82**	**$<$10e-4**	**0.81**	**$<$10e-4**	**0.82**	**$<$10e-4**
FOOOF, downsampling	0.56	$<$10e-4	0.57	$<$10e-4	0.59	$<$10e-4

Table S8: All four DOC patients whose EEG recordings were analyzed in this paper received painkillers and anesthetics as part of their treatment protocol. Unfortunately, it was not possible to determine the exact timing of drug administration relative to behavioral assessment using the Glasgow Coma Scale (GCS) and corresponding EEG recordings, and so our results for these patients could be confounded by the effects of these drugs. Here, we list the drugs that were administered to each patient *on the same day as* GCS scoring and corresponding EEG recordings, which are the only data that are available regarding the relative timing of drug administration and GCS assessment.

Subjects	Unconscious	Conscious
1	Propofol, ketamine, dexmedetomidine	none
2	Propofol, opioids, ketamine, dexmedetomidine, benzodiazepines	none
3	Propofol, opioids, ketamine, dexmedetomidine, barbituates, benzodiazepines	Propofol, opioids, ketamine, dexmedetomidine, benzodiazepines
4	Propofol, opioids, ketamine, dexmedetomidine, barbituates	Propofol, opioids, ketamine, dexmedetomidine, barbituates

SUPPLEMENTARY NOTES

Supplementary Note 1

While "chaos" and "disorder" have often been used interchangeably in the literature on neural criticality, this is in fact misleading: counter-intuitively, chaos is in fact the "ordered" phase of a dynamical system with respect to edge-of-chaos criticality[23,24]. This is because a phase is considered "ordered" with respect to a critical point if it is characterized by whatever symmetry is broken at that critical point, and it is known that the topological or de-Rham supersymmetry of dynamical systems is broken at the periodic-to-chaotic transition[23–30]. A more intuitive example of this is ice water, which is "ordered" because it lacks the translational and rotational symmetry that makes liquid water "disordered." In other words, because liquid water is disordered, any rotation or translation (along any axis) would preserve the shape of the water, meaning that it has both translational and rotational symmetry; in contrast, because ice water has a regular crystalline lattice structure, that structure will only be preserved for a limited number of rotations or translations, which means that ice water lacks translational and rotational symmetry. This lack of symmetry is what makes ice water "ordered." Similarly, because periodic systems are topologically symmetric and because this symmetry is broken at the edge-of-chaos critical point, chaos is in fact the "ordered" phase of dynamical systems. Moreover, it is important to note that this topological or de-Rham supersymmetry can be broken either by the non-integrability of a dynamical system (which is the classic definition of chaos in the deterministic sense) *or* by noise-induced tunneling between attractors (which extends the notion of chaos to stochastic dynamical systems)[23–30]. Thus, our finding that low-frequency cortical electrodynamics are weakly chaotic during conscious states is both fully consistent (if counter-intuitively so) with the proposal that waking cortical dynamics operate on the ordered side of a critical point, and with the presence of dynamic noise in cortical networks.

Supplementary Note 2

We suggest a follow-up experiment to a result reported here, which is that the mean-field model of

cortical electrodynamics exhibited its maximally information-rich, nearest-to-criticality behavior when there was a moderate reduction in the strength of gap junction coupling between inhibitory interneurons, as well as an increase in postsynaptic excitability - a parameter change which led to reduced spectral power at low frequencies (Fig. S2, S4), recapitulating results observed for the MEG recordings from humans following administration of LSD (Fig. S2, S4). This potentially points to an as-yet-unstudied molecular effect of psychedelics. It is already known that psychedelics induce a marked increase in the frequency and amplitude of spontaneous glutamatergic excitatory postsynaptic potentials in cortical layer V pyramidal cells[31–34], which leads to reduced low-frequency local field potential[35] and MEG power[36], and that an increase in cortical excitability in mean-field models can recreate many of the effects of psychedelics on macro-scale cortical dynamics[36,37]. But, there is currently no published research on the effect of psychedelics on cortical gap junction coupling[38]. That said, in light of both our simulation-based results and prior empirical findings, we predict an inhibitory effect of psychedelics on gap junction coupling. To begin, it is already known that serotonin and other 5-HT2A receptor agonists suppress gap junction coupling, and that 5-HT2A receptor antagonists attenuate this effect[39]. Additionally, the antipsychotic drugs clozapine and haloperidol, which both diminish or block the effects of psychedelics[40–42], have been shown to increase the strength of gap junction coupling[43]. Finally, psychedelics are known to bear a number of striking resemblances to the antimalarial drug mefloquine, which, like psychedelics, is a potent agonist of the 5-HT2a receptor[38], reduces low-frequency electroencephalography power[44], and can induce hallucinations and other psychiatric events[45]; importantly, mefloquine is also known to block several connexins[46–48] and is used to block gap junction coupling in experimental settings[49]. Thus, based on both our mean-field modeling results and prior empirical literature, we predict that psychedelics moderately block cortical gap junction coupling - a prediction that will need to be tested in future work.

Supplementary References

1. Bennett, M. V. & Zukin, R. S. Electrical coupling and neuronal synchronization in the mammalian brain. *Neuron* **41**, 495–511 (2004).

2. Steyn-Ross, M. L., Steyn-Ross, D. A. & Sleigh, J. W. Interacting Turing-Hopf instabilities drive symmetry-breaking transitions in a mean-field model of the cortex: a mechanism for the slow oscillation. *Physical Review X* **3**, 021005 (2013).

3. Toker, D., Sommer, F. T. & D'Esposito, M. A simple method for detecting chaos in nature. *Communications biology* **3**, 1–13 (2020).

4. Ihle, M. *et al.* EPILEPSIAE–A European epilepsy database. *Computer methods and programs in biomedicine* **106**, 127–138 (2012).

5. Dominguez, L. G. *et al.* Enhanced synchrony in epileptiform activity? Local versus distant phase synchronization in generalized seizures. *Journal of neuroscience* **25**, 8077–8084 (2005).

6. Nagasaka, Y., Shimoda, K. & Fujii, N. Multidimensional recording (MDR) and data sharing: an ecological open research and educational platform for neuroscience. *PloS one* **6**, e22561 (2011).

7. Carhart-Harris, R. L. *et al.* Neural correlates of the LSD experience revealed by multimodal neuroimaging. *Proceedings of the National Academy of Sciences* **113**, 4853–4858 (2016).

8. Crone, J. S., Bio, B. J., Vespa, P. M., Lutkenhoff, E. S. & Monti, M. M. Restoration of thalamo-cortical connectivity after brain injury: recovery of consciousness, complex behavior, or passage of time? *Journal of neuroscience research* **96**, 671–687 (2018).

9. Crone, J. S., Lutkenhoff, E. S., Vespa, P. M. & Monti, M. M. A systematic investigation of the association between network dynamics in the human brain and the state of consciousness. *Neuroscience of consciousness* **2020**, niaa008 (2020).

10. Ramasubramanian, K. & Sriram, M. A comparative study of computation of Lyapunov spectra with different algorithms. *Physica D: Nonlinear Phenomena* **139**, 72–86 (2000).

11. Donoghue, T. *et al.* Parameterizing neural power spectra into periodic and aperiodic components. *Nature neuroscience* **23**, 1655–1665 (2020).

12. Chander, D., García, P. S., MacColl, J. N., Illing, S. & Sleigh, J. W. Electroencephalographic variation during end maintenance and emergence from surgical anesthesia. *PloS one* **9**, e106291 (2014).

13. Long, C. W., Shah, N. K., Loughlin, C., Spydell, J. & Bedford, R. F. A comparison of EEG determinants of near-awakening from isoflurane and fentanyl anesthesia. Spectral edge, median power frequency, and delta ratio. *Anesthesia and analgesia* **69**, 169–173 (1989).

14. Wang, Y., Liang, Z., Voss, L. J., Sleigh, J. W. & Li, X. Multi-scale sample entropy of electroencephalography during sevoflurane anesthesia. *Journal of clinical monitoring and computing* **28**, 409–417 (2014).

15. Costa, M., Goldberger, A. L. & Peng, C.-K. Multiscale entropy analysis of biological signals. *Physical review E* **71**, 021906 (2005).

16. Lendner, J. D. *et al.* An electrophysiological marker of arousal level in humans. *Elife* **9**, e55092 (2020).

17. Gao, R., Peterson, E. J. & Voytek, B. Inferring synaptic excitation/inhibition balance from field potentials. *Neuroimage* **158**, 70–78 (2017).

18. Schartner, M. *et al.* Complexity of multi-dimensional spontaneous EEG decreases during propofol induced general anaesthesia. *PloS one* **10**, e0133532 (2015).

19. Schartner, M. M., Carhart-Harris, R. L., Barrett, A. B., Seth, A. K. & Muthukumaraswamy, S. D. Increased spontaneous MEG signal diversity for psychoactive doses of ketamine, LSD and psilocybin. *Scientific Reports* **7**, 46421 (2017).

20. Brito, M. A., Li, D., Mashour, G. A. & Pal, D. State-Dependent and Bandwidth-Specific Effects of Ketamine and Propofol on Electroencephalographic Complexity in Rats. *Frontiers in Systems Neuroscience* **14**, 50 (2020).

21. Petraitis, P., Beaupre, S. & Dunham, A. ANCOVA: nonparametric and randomization approaches. *Design and analysis of ecological experiments. Oxford University Press, New York* 116–133 (2001).

22. Eyébé Fouda, J. S. A., Bodo, B., Sabat, S. L. & Effa, J. Y. A modified 0-1 test for chaos detection in oversampled time series observations. *International Journal of Bifurcation and Chaos* **24**, 1450063 (2014).

23. Ovchinnikov, I. V. *et al.* Criticality or Supersymmetry Breaking? *Symmetry* **12**, 805 (2020).

24. Ovchinnikov, I. Introduction to supersymmetric theory of stochastics. *Entropy* **18**, 108 (2016).

25. Ovchinnikov, I. V., Schwartz, R. N. & Wang, K. L. Topological supersymmetry breaking: The definition and stochastic generalization of chaos and the limit of applicability of statistics. *Modern Physics Letters B* **30**, 1650086 (2016).

26. Parisi, G. & Sourlas, N. Random magnetic fields, supersymmetry, and negative dimensions. *Physical Review Letters* **43**, 744 (1979).

27. Parisi, G. & Sourlas, N. Supersymmetric field theories and stochastic differential equations. *Nuclear Physics B* **206**, 321–332 (1982).

28. Gozzi, E. & Reuter, M. Classical mechanics as a topological field theory. *Physics Letters B* **240**, 137–144 (1990).

29. Ovchinnikov, I. V. Topological field theory of dynamical systems. *Chaos: An Interdisciplinary Journal of Nonlinear Science* **22**, 033134 (2012).

30. Ovchinnikov, I. V. & Ensslin, T. A. Kinematic dynamo, supersymmetry breaking, and chaos. *Physical Review D* **93**, 085023 (2016).

31. Aghajanian, G. & Marek, G. Serotonin induces excitatory postsynaptic potentials in apical dendrites of neocortical pyramidal cells. *Neuropharmacology* **36**, 589–599 (1997).

32. Puig, M. V., Celada, P., Díaz-Mataix, L. & Artigas, F. In vivo modulation of the activity of pyramidal neurons in the rat medial prefrontal cortex by 5-HT2A receptors: relationship to thalamocortical afferents. *Cerebral Cortex* **13**, 870–882 (2003).

33. Nichols, D. E. Psychedelics. *Pharmacological reviews* **68**, 264–355 (2016).

34. Béïque, J.-C., Imad, M., Mladenovic, L., Gingrich, J. A. & Andrade, R. Mechanism of the 5-hydroxytryptamine 2A receptor-mediated facilitation of synaptic activity in prefrontal cortex. *Proceedings of the National Academy of Sciences* **104**, 9870–9875 (2007).

35. Wood, J., Kim, Y. & Moghaddam, B. Disruption of prefrontal cortex large scale neuronal activity by different classes of psychotomimetic drugs. *Journal of Neuroscience* **32**, 3022–3031 (2012).

36. Muthukumaraswamy, S. D. *et al.* Broadband cortical desynchronization underlies the human psychedelic state. *Journal of Neuroscience* **33**, 15171–15183 (2013).

37. Deco, G. *et al.* Whole-brain multimodal neuroimaging model using serotonin receptor maps explains non-linear functional effects of LSD. *Current Biology* **28**, 3065–3074 (2018).

38. Janowsky, A. *et al.* Mefloquine and psychotomimetics share neurotransmitter receptor and transporter interactions in vitro. *Psychopharmacology* **231**, 2771–2783 (2014).

39. Rörig, B. & Sutor, B. Serotonin regulates gap junction coupling in the developing rat somatosensory cortex. *European Journal of Neuroscience* **8**, 1685–1695 (1996).

40. Marona-Lewicka, D. & Nichols, D. E. Potential serotonin 5-HT1A and dopamine D4 receptor modulation of the discriminative stimulus effects of amphetamine in rats. *Behavioural pharmacology* **22**, 508 (2011).

41. Vollenweider, F. X., Vollenweider-Scherpenhuyzen, M. F., Bäbler, A., Vogel, H. & Hell, D. Psilocybin induces schizophrenia-like psychosis in humans via a serotonin-2 agonist action. *Neuroreport* **9**, 3897–3902 (1998).

42. Moreno, J. L. *et al.* Persistent effects of chronic clozapine on the cellular and behavioral responses to LSD in mice. *Psychopharmacology* **225**, 217–226 (2013).

43. Onn, S.-P. & Grace, A. A. Repeated treatment with haloperidol and clozapine exerts differential effects on dye coupling between neurons in subregions of striatum and nucleus accumbens. *Journal of Neuroscience* **15**, 7024–7036 (1995).

44. Franco-Pérez, J., Ballesteros-Zebadúa, P. & Manjarrez-Marmolejo, J. Anticonvulsant effects of mefloquine on generalized tonic-clonic seizures induced by two acute models in rats. *BMC neuroscience* **16**, 7 (2015).

45. Sturkenboom, M., Pepplinkhuizen, L., Stricker, B. *et al.* Mefloquine increases the risk of serious psychiatric events during travel abroad: a nationwide case-control study in the Netherlands. *The Journal of clinical psychiatry* **66**, 199–204 (2005).

46. Cruikshank, S. J. *et al.* Potent block of Cx36 and Cx50 gap junction channels by mefloquine. *Proceedings of the National Academy of Sciences* **101**, 12364–12369 (2004).

47. Iglesias, R. *et al.* P2X7 receptor-Pannexin1 complex: pharmacology and signaling. *American Journal of Physiology-Cell Physiology* **295**, C752–C760 (2008).

48. Wang, Y. *et al.* Neuronal Gap Junctions Are Required for NMDA Receptor–Mediated Excitotoxicity: Implications in Ischemic Stroke. *Journal of neurophysiology* **104**, 3551–3556 (2010).

49. Sarihi, A. *et al.* Cell type-specific, presynaptic LTP of inhibitory synapses on fast-spiking GABAergic neurons in the mouse visual cortex. *Journal of Neuroscience* **32**, 13189–13199 (2012).